On the 3D structure of Anticyclonic Eddies from *In situ* Data

Yan Barabinot[1], Sabrina Speich[1], Xavier Carton[2]

[1]Ecole Normale Supérieure, Laboratoire de Météorologie Dynamique (LMD), 24 rue Lhomond, Paris 75005, France
[2]Université de Bretagne Occidentale (UBO), Laboratoire d'Océanographie Physique et Spatiale (LOPS), IUEM, rue Dumont Durville, Plouzané 29280, France

Key Points:

- We propose a novel theoretical framework for decomposing the potential density field within the cores of ocean mesoscale eddies.
- The 3D morphology of six anticyclonic eddies sampled during the EUREC4A-OA, METEOR 124, and PHYSINDIEN 2011 in situ experiments is analyzed.
- The slope of isopycnals emerges as the predominant contributor to the overall density anomaly and exhibits a nearly Gaussian shape.

Corresponding author: Yan Barabinot, yan.barabinot@ens-paris-saclay.fr

Abstract

Mesoscale eddies are ubiquitous in the global ocean. Most of them are materially coherent: they advect a different water mass in their core than in the surrounding water, according to studies based on *in situ* observations and Lagrangian techniques. In parallel, laboratory experiments have shown that eddies have the ability to locally modify the stratification according to the thermal wind balance, without necessarily contain heterogeneous water. These two types of density anomalies associated with mesoscale eddies are often erroneously confused in the literature. Here we propose a new theoretical decomposition of the potential density field in the core of eddies to assess their respective amplitude and dynamical effect. This allows the modelling of their 3D shape and the estimation of the importance of each term. This decomposition is applied to 6 anticyclonic eddies sampled during the EUREC4A-OA, METEOR 124 and PHYSINDIEN 2011 *in situ* experiments. We show that the anomaly corresponding to the slope of the isopycnals is the largest contributor to the total density anomaly. Its vertical shape is nearly Gaussian, but also depends on the local background stratification. The horizontal density gradient associated with the trapped water mass adds a second order term to the total anomaly and can be neglected for the study of eddy dynamics. The horizontal structures of the eddies studied are consistent with previous studies and show an exponential-alpha shape.

Plain Language Summary

Mesoscale eddies are ubiquitous rotating currents in the ocean. They are considered one of the most important sources of ocean variability because they can live for months and transport heat, salt, and other properties within and between ocean basins. They have been studied extensively from satellite observations because a number of them are at or near the ocean surface. However, observations and analyses of their 3D structure are rare, and calculations of eddy transport are often approximated without precise knowledge of their true vertical extent. Here, we propose a new theoretical framework based on the theory of geophysical fluid dynamics and apply it to observations collected during field experiments in order to quantitatively determine the 3D shape of mesoscale eddies.

1 Introduction

Ocean dynamics are highly nonlinear and are characterized by physical processes that give rise to features across a wide range of spatial scales, from 1,000 km to 1 km and even smaller. Among these features are mesoscale eddies, which refer to coherent structures that typically have spatial scales of 10-200 km and time scales of 10-100 days (Carton, 2001; D. Chelton et al., 2011; Morrow & Traon, 2012). Mesoscale eddies influence all the different dynamical components of the ocean, from air-sea fluxes (e.g., Frenger et al., 2013) to ventilation of the deep interior (Sallée et al., 2010) and large-scale ocean circulation (Morrow et al., 1994; Lozier, 1997). In addition, they are thought to play an important role in the transport of heat, salt, carbon, and chemical constituents as they propagate in the ocean, and thus represent a key dynamical element in the global budgets of these tracers (Bryden, 1979; Jayne & Marotzke, 2002; Morrow & Traon, 2012; Wunsch, 1999).

Mesoscale eddies are energetic features, mostly constrained in the horizontal plane by planetary rotation and ocean thermohaline stratification. They occur in different shapes and are generated by a variety of mechanisms (Carton, 2001; Carton et al., 2010). They have a major influence on the propagation of tracers by advecting them over long distances and times (McWilliams, 1985). The lifetime of such structures often exceeds several months and can reach several years (Laxenaire et al., 2018; Chaigneau et al., 2009).

In an attempt to reproduce these structures, numerical simulations and laboratory experiments have shown that eddies in a rotating stratified medium have a longer lifetime than those in a non-rotating homogeneous medium (McWilliams, 1984, 1989, 1990; Aubert et al., 2012). These studies suggest two reasons for the longevity of isolated oceanic eddies (also known as mesoscale eddies). First, because stratification horizontally confines the velocity field and the rotating flow is mostly 2D, energy cascades upscale, favoring the development of large eddies (Kolmogorov, 1941; McWilliams, 1984). Second, in a stratified medium, the rotating flow of vortices is mostly controlled by the thermal wind balance (Douglass & Richman, 2015; Cao et al., 2023; Penven et al., 2014). By modifying the local stratification, a vortex induces a radial buoyancy gradient that balances the vertical velocity gradient (if the centrifugal force is neglected, which is the case when the Rossby number is less than unity) as long as the buoyancy anomaly exists. Therefore, in the absence of dissipation processes, the buoyancy anomaly persists and so does the rotating flow. Even in the presence of viscosity, the stratification acts as a backbone for the flow, making its damping weaker than for non-stratified flow.

In such vortices, when the flow trajectories are closed and lateral intrusion can be neglected, a mass of water is trapped in the core. This water mass is characteristic of the vortex formation area. It can then be advected away from the formation region (Flierl, 1981; Beron-Vera et al., 2013; Haller, 2015). Recent studies have shown that on isopycnic surfaces, both anticyclonic and cyclonic eddies can exhibit positive or negative anomalies of temperature and salinity fields (Aguedjou et al., 2021; Cui et al., 2021; Lin et al., 2019). However, the effect of such anomalies on the dynamical properties of eddies remains poorly understood. Conversely, some eddies in experimental studies have been associated not with thermohaline anomalies on isopycnals, but with vertical deviations of these isopycnals from a quiescent state. In fact, thermohaline anomalies appearing on isopycnals are a consequence of a difference in water masses between the core and the surrounding area. They can occur either because of eddy drift or because the thermohaline properties of the region of interest change while the eddy remains stationary. As a result, previous studies have completely disentangled the two effects, although they are decorrelated.

In addition, with the advent of satellite altimetry, many studies over the last 20 years have been devoted to the general assessment of the characteristics and propagation properties of mesoscale eddies in the upper ocean (e.g., D. B. Chelton et al., 2007; D. Chelton et al., 2011; Chaigneau et al., 2008). These studies have made considerable progress in understanding eddy dynamics from a 2D (sea surface) perspective, but very little has been done to characterize their vertical structures. To improve our knowledge of global ocean eddies, recent studies have attempted to systematically combine satellite altimetry observations of eddies with vertical profiles from Argo floats to obtain 3D eddy reconstructions using composite methods (e.g., Chaigneau et al., 2011; Souza et al., 2011; B. Yang et al., 2021; Pegliasco et al., 2015; Nencioli et al., 2018; Laxenaire et al., 2019, 2020). These methods allow for long time series of thermohaline anomalies in the eddy core and help to quantify heat and salt transport. However, they often aim to reconstruct an average structure of an eddy with profiles taken at different times of the eddy's life cycle, which is not suitable for studying its true structure and evolution. In particular, no work has been devoted to understanding and quantifying the 3D shape of the density anomaly in the eddy core, which is key to reconstructing the velocity field and thus understanding eddy stability, flow trajectories, and estimating eddy coherence.

In this paper, we consider a hydrological approach to mesoscale eddies as opposed to a dynamical view based on the flow field. The first reason is that we consider a scalar field (density) instead of a vector field (velocity), which is easier to measure with current physical oceanography devices, and the second reason is that the detailed method can be applied on Argo floats, which remain powerful devices for sampling the 3D hydrological structure of eddies (especially their vertical extension). Therefore, in this vi-

sion, the background stratification is considered as the skeleton of mesoscale eddies. Based on theoretical considerations, we decompose the potential density field in the eddy core into three components. Each component is analyzed and two are identified as the density anomaly associated with the eddy structure. The magnitudes are calculated and analytical functions are estimated to model their shape. Then, using *in situ* data of 6 anticyclonic eddies sampled during EUREC4A-OA, METEOR 124 and PHYSIENDIEN 2011 and an optimization algorithm, we show how the analytical models fit the data. Finally, based on the results, an expression to model the potential density anomaly is proposed and discussed. Note that due to lack of data, this study is limited to anticyclonic eddies even if the theoretical part can also be applied for cyclonic eddies.

2 Theoretical Framework

2.1 Potential density field decomposition

Let us consider an isolated and materially coherent vortex. So we consider a cylindrical frame of reference. Since two water masses of equal density will not have the same T/S values, we can separate the trapped water mass from the surrounding water by calculating the thermohaline anomalies on the isopycnals $\Delta_{\sigma_0}T$ and $\Delta_{\sigma_0}S$, with respect to a reference profile. Given $\overline{T}$ and $\overline{S}$ two reference profiles in temperature and salinity (outside the eddies) and T and S *in situ* temperature and salinity profiles (inside the eddies at a distance r from the center and oriented at an angle θ), thermohaline anomalies on isopycnals are computed as follows:

$$\forall\sigma_0, \quad \Delta_{\sigma_0}T(r,\theta,\sigma_0) = T(r,\theta,\sigma_0) - \overline{T}(\sigma_0) \tag{1}$$
$$\forall\sigma_0, \quad \Delta_{\sigma_0}S(r,\theta,\sigma_0) = S(r,\theta,\sigma_0) - \overline{S}(\sigma_0) \tag{2}$$

where σ_0 is the potential density field at atmospheric pressure. These anomalies quantify how much T and S vary when following an isopycnal. They are used to quantify the amount of heat and salt transported by the eddy (Laxenaire et al., 2019; Y. Yang et al., 2021).

Now let us construct $\hat{T}/\hat{S}$ fields such that these thermohaline anomalies on isopycnals have been removed from the *in situ* T/S fields. This subtraction must be computed on geopotential levels z such that:

$$\forall z, \quad \hat{T}(r,\theta,z) = T(r,\theta,z) - \Delta_{\sigma_0}T(z) \tag{3}$$
$$\forall z, \quad \hat{S}(r,\theta,z) = S(r,\theta,z) - \Delta_{\sigma_0}S(z) \tag{4}$$

Thus, we obtain two fields without the deviation on isopycnals of the temperature and salinity fields. The thermohaline contribution of the trapped water has been removed on geopotential levels, and we obtain a fictive eddy structure for which the water masses in and out of the core have the same properties. Following an isopycnal, the $\hat{T}/\hat{S}$ fields are such that each isopycnal is associated with a unique isotherm and a unique isohaline.

The temperature and salinity fields are important for studying eddy diffusion and transport. However, what is most important for eddy dynamics is the density. For a given T/S field, the associated potential density σ_0 at atmospheric pressure is given by a complex nonlinear function, which we call F, such that:

$$\sigma_0 = F(T,S) \tag{5}$$

Here σ_0 is directly the deviation from the water density $1000kg/m^3$. In practice, this quantity is calculated using the TEOS-10 standard (McDougall et al., 2003; Roquet et al., 2015). In this expression, with the previous equations, we can introduce the $\hat{T}/\hat{S}$ fields and develop using a Taylor expansion:

$$\begin{aligned}
\sigma_0 &= F(\hat{T} + \Delta_{\sigma_0} T, \hat{S} + \Delta_{\sigma_0} S) && (6)\\
&= F(\hat{T}, \hat{S}) + \left(\frac{\partial F}{\partial T}\right)_{S,z} \Delta_{\sigma_0} T + \left(\frac{\partial F}{\partial S}\right)_{S,z} \Delta_{\sigma_0} S + O(\Delta_{\sigma_0} T) + O(\Delta_{\sigma_0} S) && (7)\\
&= \hat{\sigma_0} + \delta^2 \sigma_0 && (8)
\end{aligned}$$

with,

$$\begin{aligned}
\hat{\sigma_0} &= F(\hat{T}, \hat{S}) && (9)\\
\delta^2 \sigma_0 &= \left(\frac{\partial F}{\partial T}\right)_{S,z} \Delta_{\sigma_0} T + \left(\frac{\partial F}{\partial S}\right)_{S,z} \Delta_{\sigma_0} S + O(\Delta_{\sigma_0} T) + O(\Delta_{\sigma_0} S) && (10)
\end{aligned}$$

Physically, $\delta^2\sigma_0$ is the component of the potential density field resulting from the difference in water masses between the core and the ambient. In practice, it can be obtained by subtracting $\hat{\sigma_0}$ from σ_0 at geopotential levels. As shown in equation (10), it depends directly on the thermohaline anomalies on the isopycnals. The more the trapped water is different, the more this term is high. Since the eddy is mostly in hydrostatic equilibrium, the effects of temperature and salinity anomalies often cancel each other out, and we expect this component to be small. However, we expect this term to be non-negligible for mesoscale eddies that have large differences in water masses with their surroundings. This may be the case for meddies because the Mediterranean Water they transport is very different from that of the Atlantic Ocean (Tychensky & Carton, 1998). $\delta^2\sigma_0$ is the first contribution to the baroclinic term of the potential density anomaly.

When calculating $\hat{\sigma_0}$, there is no reason for the isopycnals to be flat in the rest state (i.e., without the presence of the eddy). As a result, by subtracting the reference profile of the potential density $\overline{\sigma_0}$ from $\hat{\sigma_0}$ at geopotential levels, there exists a resulting term $\delta\sigma_0$ such that:

$$\forall z \quad \delta\sigma_0(r,\theta,z) = \hat{\sigma_0}(r,\theta,z) - \overline{\sigma_0}(z) \tag{11}$$

Physically, this term expresses the deviation of the isopycnals from their rest state when the contribution of trapped water is removed. This is the second contribution to the baroclinic term of the potential density. In practice, it can be calculated at geopotential levels according to equation (11). Finally, for each geopotential level, the potential density σ_0 can be decomposed into three contributions (see figure 1):

$$\sigma_0(r,\theta,z) = \overline{\sigma_0}(z) + \delta\sigma_0(r,\theta,z) + \delta^2\sigma_0(r,\theta,z) \tag{12}$$

2.2 Density Anomaly Formulation

In this section, we use geophysical fluid dynamics arguments to determine orders of magnitude for both terms in the potential density anomaly decomposition.

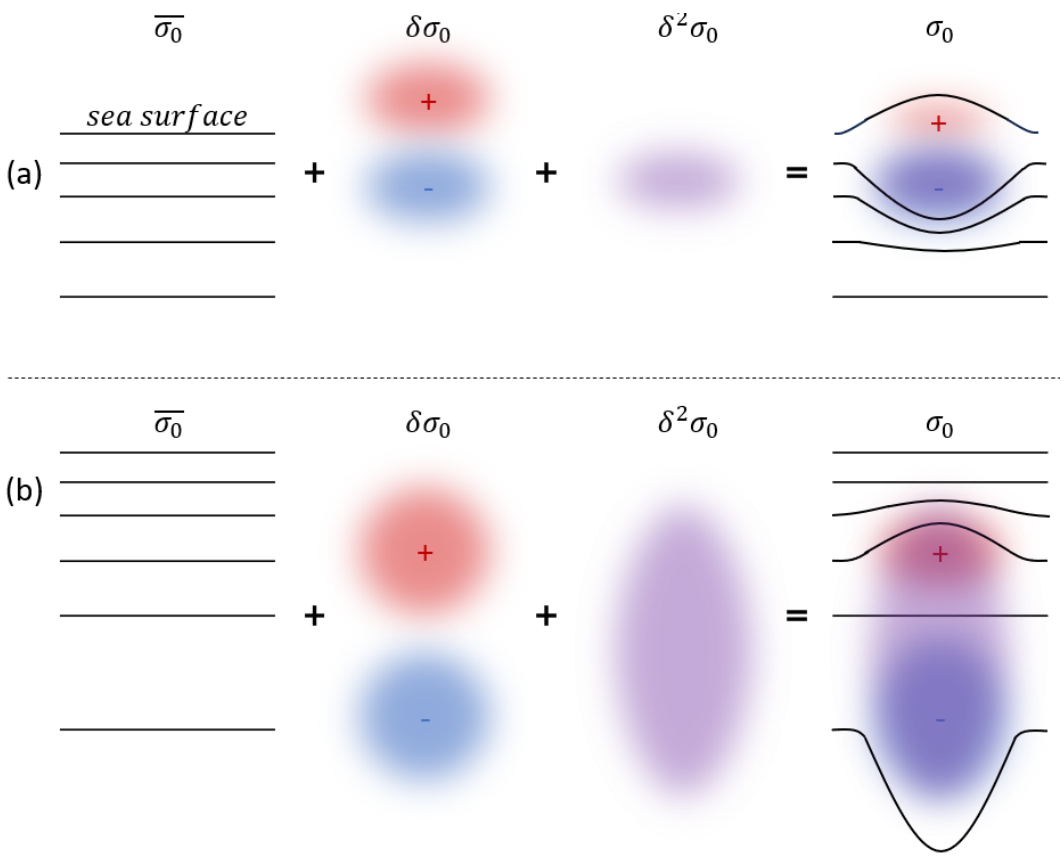

Figure 1. Sketch showing the three components of the potential density field for a surface (a) and a subsurface (b) anticyclonic eddy. $\overline{\sigma_0}$ is the background stratification (each dark line is an isopycnal), $\delta\sigma_0$ is the anomaly associated with the displacement of the isopycnals, and $\delta^2\sigma_0$ is the anomaly associated with the trapped water properties. Together they form the total *in situ* field σ_0. The location where the isopycnals do not deviate is called the median plane of the eddy.

2.2.1 Expression for $\delta\sigma_0$

We recall that this component can be thought of as the deviation of the isopycnals from their state at rest when the contribution of trapped water has been removed. Consider a stratified ocean at rest where the temperature, salinity, and potential density are the climatological averages $\overline{T}(z)$, $\overline{S}(z)$, and $\overline{\sigma_0}(z)$. This ocean is assumed to be in hydrostatic equilibrium with no fronts, incropping or outcropping. Therefore the relation $\overline{\sigma_0}(z)$ is one-to-one and invertible. Let us call $\overline{Z}$ the reciprocal such that $z = \overline{Z}(\overline{\sigma_0}(z))$.

Then we assume that isopycnals, isothermals, and isohalines are dynamically deviated without introducing thermohaline anomalies on isopycnals. In cylindrical coordinates, $\eta(r,\theta,\sigma_0)$, $\eta_T(r,\theta,\sigma_0)$, and $\eta_S(r,\theta,\sigma_0)$ are the deviations of isopycnals, isothermals, and isohalines, respectively, with respect to their state of rest, temperature, salinity, and potential density fields:

$$T(r,\theta,z) = \overline{T}(z+\eta_T(r,\theta,\sigma_0)) \quad (13)$$
$$S(r,\theta,z) = \overline{S}(z+\eta_S(r,\theta,\sigma_0)) \quad (14)$$
$$\sigma_0(r,\theta,z) = \overline{\sigma_0}(z+\eta(r,\theta,\sigma_0)) \quad (15)$$

Following isopycnal σ_{01}, we have $\sigma_0(r,\theta,z) = \sigma_{01}$ and thus:

$$z(r,\theta,\sigma_{01}) = \overline{Z}(\sigma_{01}) - \eta(r,\theta,\sigma_{01}) \tag{16}$$

which represents the geopotential level of the perturbed isopycnal σ_{01}. As a result, one can write the expression of $\sigma_0(r,\theta,z)$ as follows:

$$\sigma_0(r,\theta,z(r,\theta,\sigma_{01})) = \overline{\sigma_0}(\overline{Z}(\sigma_{01}) - \eta(r,\theta,\sigma_{01})) \tag{17}$$

which gives at first order :

$$\sigma_0(r,\theta,z(r,\sigma_{01})) = \sigma_{01} - \eta(r,\theta,\sigma_{01})\frac{d\overline{\sigma_0}}{dz}(\overline{Z}(\sigma_{01})) \tag{18}$$

And finally,

$$\delta\sigma_0(r,\theta,z) = \sigma_0(r,\theta,z(r,\sigma_{01})) - \sigma_{01} = -\eta(r,\theta,\sigma_{01})\frac{d\overline{\sigma_0}}{dz}(\overline{Z}(\sigma_{01})) \tag{19}$$

We recover the relationship of (Bretherton, 1966) for potential density anomalies produced by isopycnal displacement. We clearly see that the background stratification plays a role in determining both the values and the vertical shape of $\delta\sigma_0$. As a result, if we introduce h, the scale for η, $\delta\sigma_0$ scales as follows:

$$\delta\sigma_0 = h\frac{\Delta\overline{\sigma_0}}{\Delta z} \tag{20}$$

The vertical gradient of $\overline{\sigma_0}$ depends on the region and whether the eddy is surface or subsurface intensified. For a surface intensified eddy, assuming a classical variation of $1kg/m^3$ for $100m$ depth at rest and a characteristic deviation of $100m$, $\delta\sigma_0 = 1kg/m^3$. For a subsurface eddy like the one in figure 4, assuming a variation of $0.5kg/m^3$ for $200m$ depth at rest and a characteristic deviation of $200m$, $\delta\sigma_0 = 0.5kg/m^3$.

The same method can be applied to both temperature and salinity profiles as long as the $\overline{T}(z)$ and $\overline{S}(z)$ relations are one-to-one and invertible. Otherwise, a piecewise approach can be used to get the same result. Denoting η_T and η_S the deviation of isothermal and isohaline with respect to their rest state, Z_T and Z_S the reciprocal, one can write

$$\delta T(r,\theta,z) = -\eta_T(r,\theta,T_0)\tfrac{d\overline{T}}{dz}(\overline{Z_T}(T_0)) \tag{21}$$

$$\delta S(r,\theta,z) = -\eta_S(r,\theta,S_0)\tfrac{d\overline{S}}{dz}(\overline{Z_S}(S_0)) \tag{22}$$

for every isothermal T_0 and isohaline S_0.

2.2.2 Expression of $\delta^2\sigma_0$

In this section, we compute the effect of a different water mass in a stratified ocean at rest, where temperature, salinity, and potential density are the climatological averages $\overline{T}(z)$, $\overline{S}(z)$, and $\overline{\sigma_0}(z)$. This effect is independent of the previous one. The ocean is assumed to be in hydrostatic equilibrium, without fronts, incropping or outcropping isopycnals. For this ocean at rest, we introduce the linearized equation of state for the density as an approximation of the complex and nonlinear function F introduced previously. This equation has the following form

$$\overline{\rho}(z) = \rho_0(1 - \beta_T(\overline{T}(z) - T_0) + \beta_S(\overline{S}(z) - S_0) + \beta_P(P(z) - P_0)) \tag{23}$$

where ρ_0, T_0, and S_0 are characteristic values of the density, temperature, and salinity fields, respectively (e.g., an average over each grid point of the data), $\beta_T = O(2 \times 10^{-4})K^{-1}$ is the thermal expansion coefficient, $\beta_S = O(7.6{\times}10^{-4})ppt^{-1}$ (ppt = parts per thousand) the saline contraction coefficient, and $\beta_P = O(4{\times}10^{-10})Pa^{-1}$ the compressibility coefficient. P is the hydrostatic pressure at rest, so $P - P_0 = \rho_0 gz$. For the data, we introduce $\sigma_0 = \rho - 1000kg/m^3$ and $\sigma_0^* = \rho_0 - 1000kg/m^3$. We also note $\alpha_1 = \rho_0\beta_T$, $\alpha_2 = \rho_0\beta_T$, and $\alpha_3 = \rho_0\beta_T$, so that:

$$\overline{\sigma_0}(z) = \sigma_0^* - \alpha_1(\overline{T}(z) - T_0) + \alpha_2(\overline{S}(z) - S_0) + \alpha_3\rho_0 gz \tag{24}$$

Note that this expression does not refer to the potential density. It would be the case at first order by replacing the temperature by the conservative temperature. In our case, however, since eddies are often at the surface or just below the thermocline, the effect of compressibility is often negligible and the *in situ* density can be approximated by the first-order potential density. In the following, we will consider σ_0 as the potential density.

Now we introduce the different trapped waters so that locally (in the eddy core) the density field is written in cylindrical coordinates:

$$\sigma_0(r, \theta, z) = \sigma_0^* - \alpha_1(T(r, \theta, z) - T_0) + \alpha_2(S(r, \theta, z) - S_0) + \alpha_3\rho_0 gz \tag{25}$$

Following the isopycnal σ_{01}, we thus have:

$$\sigma_{01} = \sigma_0^* - \alpha_1(\overline{T} - T_0) + \alpha_2(\overline{S} - S_0) + \alpha_3\rho_0 gz \tag{26}$$
$$\sigma_{01} = \sigma_0^* - \alpha_1(T(r, \theta, z) - T_0) + \alpha_2(S(r, \theta, z) - S_0) + \alpha_3\rho_0 gz \tag{27}$$

Combining both equation, we obtain:

$$\alpha_1(T(r, \theta, z) - \overline{T}(z)) = \alpha_2(S(r, \theta, z) - \overline{S}(z)) \tag{28}$$

which shows that thermal and salinity anomalies compensate on isopycnals. On geopotential levels, the density anomaly associated to a different trapped water writes:

$$\delta^2\sigma_0(r, \theta, z) = -\alpha_1(T(r, \theta, z) - \overline{T}(z)) + \alpha_2(S(r, \theta, z) - \overline{S}(z)) \tag{29}$$

As before, we see that the references $\overline{T}/\overline{S}$ play a role in determining the vertical shape and values of $\delta^2\sigma_0$. Considering thermal anomalies of the order of $-1°C$ and salinity anomalies of the order of $-0.2psu$ (see figure 4), $\delta^2\sigma_0 = 0.048kg/m^3$, which is much smaller than $\delta\sigma_0$. From a theoretical point of view, the difference in water properties between the core of an eddy and its surroundings seems to play a minor role. This will be confirmed in the following section by evaluating the order of magnitude of the different terms using *in situ* observations.

2.3 Predicting the Shape of $\delta\sigma_0$ and $\delta^2\sigma_0$

The goal of this study is to understand the shape of the anomaly in the core of the eddy, in addition to the detailed decomposition of the potential density terms. Based on the previous section, the density field can be written:

$$\sigma_0(r,\theta,z) = \overline{\sigma_0}(z) - \eta(r,\theta,z)\frac{d\overline{\sigma_0}}{dz} + \delta^2\sigma_0(r,\theta,z) \tag{30}$$

Now, we assume that we can separate the variables such that:

$$\eta(r,\theta,z) = \phi(r)\varepsilon(\theta)\psi(z) \tag{31}$$
$$\delta^2\sigma_0(r,\theta,z) = \chi(r)\beta(\theta)\xi(z) \tag{32}$$

where ϕ, ε, ψ, χ, β, ξ are continuous and differentiable functions. Some expressions for the radial part can be found in the literature. For example, (Carton & McWilliams, 1989) showed that:

$$\phi(r), \chi(r) \propto \exp\left(-\left(\frac{r}{R}\right)^{\alpha}\right) \tag{33}$$

where R is the radius of the maximum velocity and α is an exponent that can vary from 2 to 3 during the lifetime of the vortex (Bennani et al., 2022; Ayouche et al., 2021). The value of 2 corresponds to the well-known Gaussian vortices. It is important to note that the two anomalies are confused in the literature, so it is difficult to say whether they have the same shape.

ε and β determine the 2D shape of the vortex. In particular, for an axisymmetric eddy, $\varepsilon = \beta = 1$. In practice, these functions can be determined from satellite data (Chen et al., 2019). However, it is almost impossible to find them from ship-based data, as we only have access to a vertical section. This is not enough to capture the 2D shape of an eddy.

ψ and ξ drive the vertical expansion of the potential density anomaly. To the best of our knowledge, neither of these functions has ever been characterized for mesoscale eddies. ψ represents the variations due to the vertical deviation of the isopycnals without the influence of the presence of a trapped water mass in the eddy core. In laboratory experiments with a constant background stratification, some studies found a Gaussian shape for the total $\delta\sigma_0$ (Flór, 1994). In fact, diffusion tends to smooth the anomaly in a self-similar way. In our case, the background stratification is not constant. However, if the stratification is constant, we should be able to recover the previous results with our formula. For an anticyclonic eddy, ψ must be positive in the shallower part of the eddy (say, above the eddy's mid-plane), but negative in the deeper part of the eddy (below the eddy's mid-plane). Taking the sign change into account, we propose from this discussion a self-similar form for ψ such that

$$\psi(z) = \psi_0\left(\frac{z-z_1}{H_1}\right)\exp\left(-\frac{(z-z_1)^2}{H_1^2}\right) \tag{34}$$

where z_1 is the geopotential level of the median plane, H_1 is a characteristic length scale, and ψ_0 is the amplitude of the signal.

On the contrary, if the confined water is homogeneous, there is no reason for ε to change sign on the vertical. The trapped water is only a patch in the eddy core. Since turbulent diffusion will affect the shape of this water mass anomaly, we propose the following self-similar expression:

$$\xi(z) = \xi_0\exp\left(-\frac{(z-z_2)^2}{H_2^2}\right) \tag{35}$$

where z_2 is the location of the maximum, H_2 is a characteristic length scale, and ξ_0 is the amplitude of the signal. The goal now is to see if these shapes fit the data well. For this purpose, we consider 6 anticyclonic eddies sampled in different regions of the global ocean to analyze their 3D structures.

3 *In situ* Data and Methods

3.1 Collection of *in situ* data

The data analyzed here were collected during 3 oceanographic cruises in 3 different parts of the world: the EUREC^{4}A-OA campaign along the north coast of Brazil, which studied mesoscale eddies and the ocean-atmosphere coupling; the FS METEOR M124 expedition, which was the first of the two SACross2016 expeditions; and the PHYSINDIEN 2011 experiment along the Omani coast (western Arabian Sea), which studied the eddy field in this area. The goal was to gather a sufficient number of eddies sampled in different regions at different times of their life cycle to study their vertical extension. To compute our diagnostics from the data, we required that the campaigns must have collected hydrological and velocity measurements of sufficient coverage of the water column. Velocities are used to locate the eddy center. The difficulty was to obtain sections close enough to the eddy center (the location where the velocity is zero) where the full vertical and radial extension of the eddies was sampled.

The EUREC^{4}A-OA campaign took place between the 20^{th} of January and the 20^{th} of February 2020 (Stevens et al., 2021; Speich & Team, 2021). We focus here on two anticyclonic eddies (hereafter AEs) sampled along the continental slope of Guyane by the French RV L'Atalante. One of the AEs is a surface intensified eddy and has been identified as an NBC ring (Subirade et al., 2023). Its velocity field extends to a depth of $-150m$. The other is a subsurface intensified anticyclone (with an intra-thermocline structure). Its core is located between -200 and -600 m depth. Hydrographic observations were made using Conductivity Temperature Pressure (CTD), underway CTD (uCTD) and Lower Acoustic Doppler Profiler (L-ADCP) measurements. A Moving Vessel Profiler (MVP) was also used to observe the surface-intensified eddy, but only for a few vertical profiles on the eastern side of the eddy (Speich & Team, 2021; L'Hégaret et al., 2022). A total of 25 and 24 CTD/uCTD profiles sampled the NBC ring and the subsurface eddy, respectively. The eddy velocity field was also measured by two ship-mounted ADCPs (S-ADCPs) with sampling frequencies of 75kHz and 38kHz. Temperature and salinity were measured by the CTD with an accuracy of $\pm 0.002°C$ and $\pm 0.005psu$, respectively. For the uCTD, the temperature and salinity accuracies are $\pm 0.01°C$ and $\pm 0.02psu$, respectively. The S-ADCP measures horizontal velocities with an accuracy of $\pm 3cm/s$. See L'Hégaret et al. (2022) for more information on the in-situ data collected during the EUREC^{4}A-OA fieldwork.

The *in situ* data were collected along sections, where stations or soundings provide vertical profiles at different distances from each other. We define the resolution of each section as the average of all distances between its successive soundings. For the particular section of the subsurface anticyclonic eddy discussed here, the hydrographic data (considering only the CTD/uCTD profiles) have a horizontal (resp. vertical) resolution of $8.4km$ (resp. $1m$) and the velocity data have a horizontal (resp. vertical) resolution of $0.3km$ (resp. $8m$ - we use the 38 kHz S-ADCP data). For the NBC ring, the data have a horizontal (resp. vertical) resolution of $10.3km$ (resp. $1m$) and the velocity data have a horizontal (resp. vertical) resolution of $0.3km$ (resp. $8m$ - we use the 38 kHz S-ADCP data). In the following, either the resolution of the hydrographic data or that of the velocity data will be used, depending on the properties of interest.

The RV Meteor M124 cruise took place between 29^{th} of February 2016 and 18^{th} of March 2016 (Karstensen et al., 2016) and crossed the South Atlantic Ocean between

Cape Town and Rio de Janeiro. We focus on 3 AE that appear to be Agulhas rings sampled in the South Atlantic Ocean near the west coast of South Africa. Each eddy is associated with an extremum of the absolute dynamic topography derived from satellite altimetry (see Figure 1 of (Karstensen et al., 2016)). These eddies extend vertically below -400 m depth. uCTD and sADCP measurements were performed to study their vertical structure. The 12, 11 and 11 uCTD profiles provide access to the thermohaline properties of the eddies. For each eddy, the hydrographic data have a horizontal (resp. vertical) resolution of $21km$ (resp. $1m$) and the velocity data have a horizontal (resp. vertical) resolution of $0.3km$ (resp. $32m$).

The Physindien 2011 experiment took place in March 2011. We focus on a surface AE sampled in the Arabian Sea near the east coast of Oman. These eddies extend vertically below -300 m depth. uCTD measurements were performed to study their vertical structure. Near 90 uCTD profiles provide access to the thermohaline properties of the AE. For each eddy, the hydrographic data have a horizontal (resp. vertical) resolution of $2km$ (resp. $1m$) and the velocity data have a horizontal (resp. vertical) resolution of $0.3km$ (resp. $16m$).

For the purpose of our study, it is important that the *in situ* section of the eddies crosses the eddy centers to avoid side effects. In Figure 2, we show, using the S-ADCP/L-ADCP data and the eddy center detection method of Nencioli et al. (2008), that this was the case for the data we used.

3.2 Data processing

For each campaign, the raw data were validated, calibrated, and then interpolated. Interpolation of vertical profiles sampled at different times had to be done carefully to avoid creating an artificial signal. To limit spurious effects, we only performed linear interpolations in $\vec{x}$ (here radial) and in $\vec{z}$ (vertical) directions. The data was then smoothed with a numerical low-pass filter of order 4 (scipy.signal.filt in Python). The choice of thresholds is subjective and depends on the scales studied. Here we consider mesoscale eddies, so we choose thresholds of the order of $L_x \approx 10km$ and $L_z \approx 10m$ for the horizontal and vertical length scales. Obviously, the cutoff period is chosen to be longer than the spatial sampling of the calibrated data. The grid size chosen for the interpolated data $(\Delta x, \Delta z)$ as well as the cutoff periods L_x and L_z are summarized in table 1 for each cruise. Figure 3 shows vertical slices of the eddy core potential density after smoothing.

Table 1. Grid size of interpolated data and cutoff periods for the 3 cruises.

Cruise	$\Delta x[km]$	$\Delta z[m]$	$L_x[km]$	$L_z[m]$
EUREC^{4}A-OA	1	0.5	10	10
M124	1	1	25	40
Phy11	1	1	10	10

3.3 Climatological averages

Our decomposition method relies on the choice of the reference profile of potential density $\overline{\sigma_0}(z)$, temperature $\overline{T}(z)$, and salinity $\overline{S}(z)$. The best choice has been the subject of several studies. One method might be to average the geopotential levels for each quantity on each uCTD/CTD profile of the respective cruise. However, the profiles may have been sampled far from each other and the water mass properties often do not match. Here, we use the methodology developed by (Laxenaire et al., 2018). A climatological average of temperature/salinity/potential density is computed over the geopotential lev-

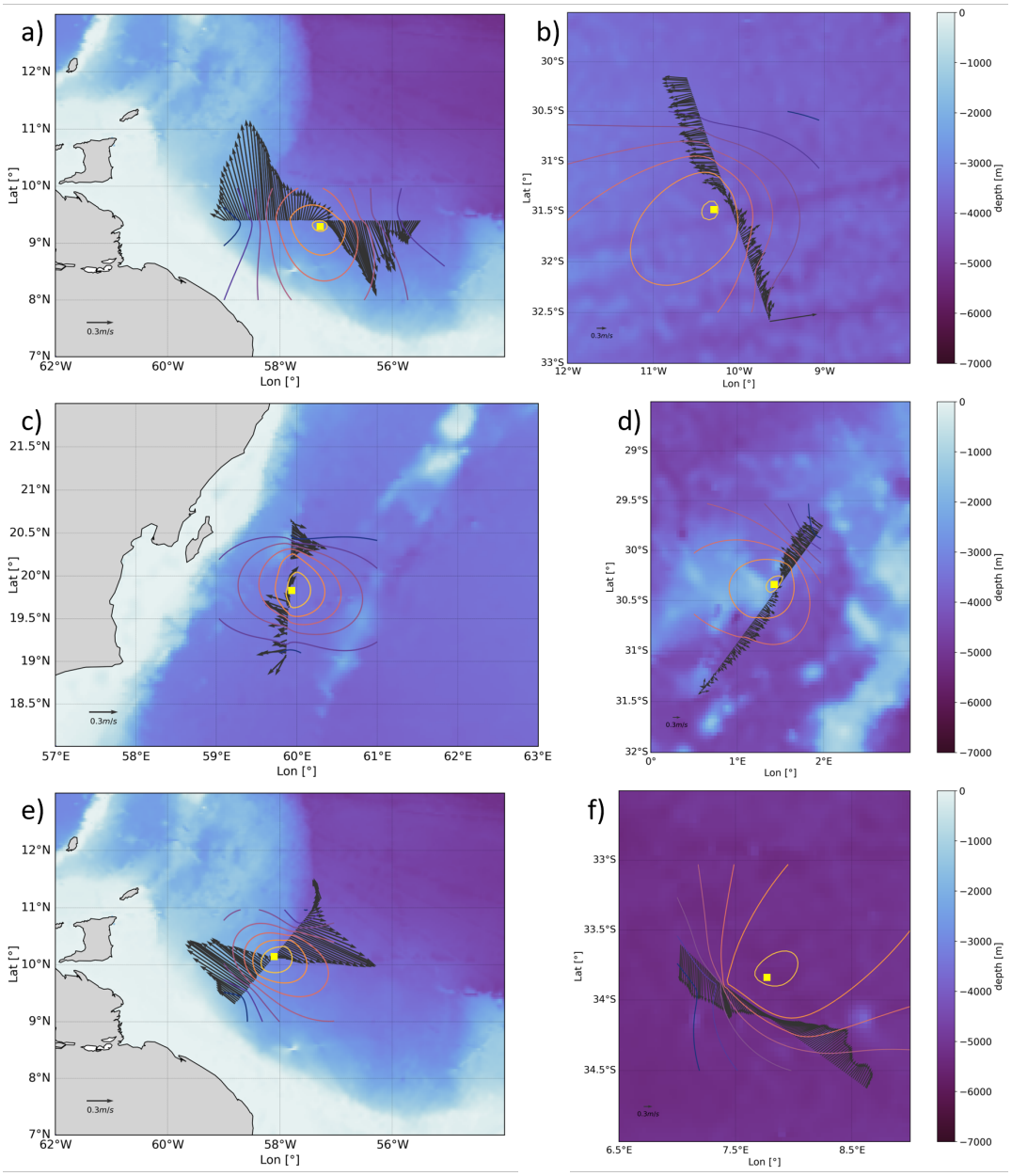

Figure 2. Velocity vector field at: $-50m$ for the surface AE of EUREC^{4}A-OA (a), $-150m$ for the first AE of M124 (b), $-50m$ for the surface AE of PHYSINDIEN 2011 (c), $-150m$ for the second AE of M124 (d), $-300m$ for the subsurface AE of EUREC^{4}A-OA (e), $-200m$ for the third AE of M124 (f). The regional bathymetry from the ETOPO2 dataset (Smith & Sandwell, 1997) is shown in the background as colored shading, as is the estimated center (the yellow square) of the eddy computed from the observed velocities using the Nencioli et al. (2008) method. The colored contours represent the loci of constant tangential velocity. The center is defined as the point where the mean radial velocity is minimum.

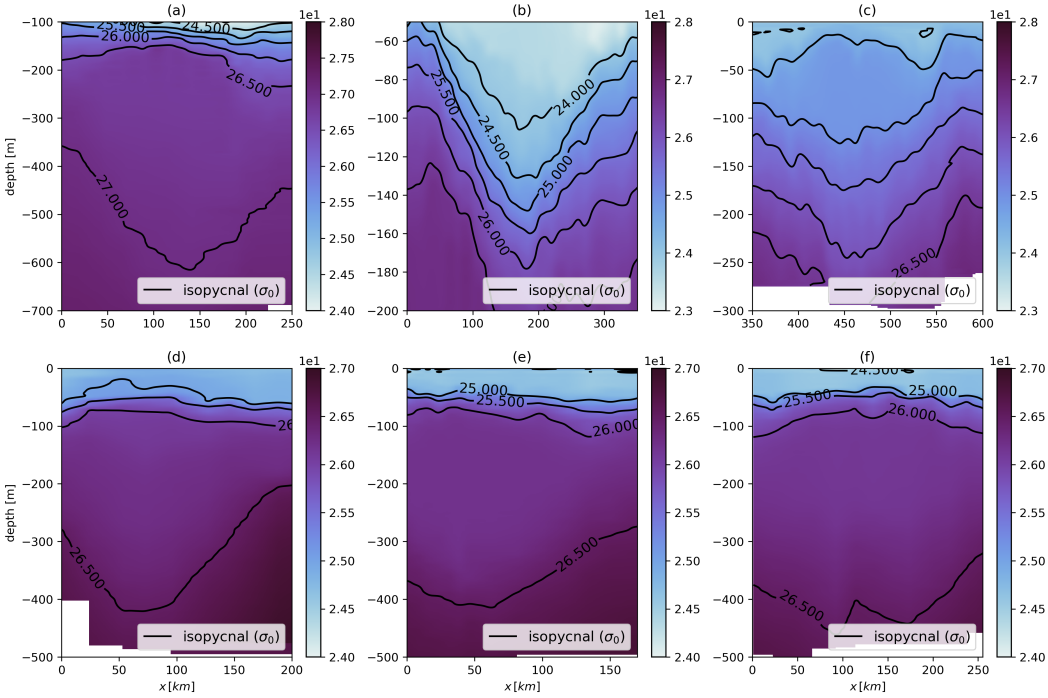

Figure 3. Vertical sections of the potential density in the eddy core. The vertical axis is the depth [m] and the horizontal axis is the horizontal scale [km]. On each panel, the dark lines are isopycnals. They are spaced in the eddy core according to their anticyclonic behavior. (a) Subsurface intensified AE from EUREC^{4}A-OA data. (b) Surface intensified AE from EUREC^{4}A-OA data. (c) Surface intensified AE from PHYSINDIEN 2011 data. (d), (e) and (f) AEs sampled during the M124 cruise.

els in a domain containing the sampled eddy. After determining the eddy center using the routine of (Nencioli et al., 2008), a square with side 0.5° is constructed around the estimated center so that it lies at the intersection of the diagonals. Then, using the Coriolis.eu.org database, all temperature, salinity, and potential density profiles sampled by Argo profiling floats over 20 years in this area are assembled and their values averaged over the geopotential levels.

3.4 Methodology for Potential Density Field Decomposition on *in situ* Data

In the case of a 2D vertical section passing through the eddy center of the horizontal axis $\vec{x}$ and the vertical axis $\vec{z}$ (as for *in situ* data collected from ships), our decomposition takes the following form:

$$\sigma_0(x,z) = \overline{\sigma_0}(z) + \delta\sigma_0(x,z) + \delta^2\sigma_0(x,z) \tag{36}$$

To compute $\delta\sigma_0$ and $\delta^2\sigma_0$, the following sequential steps are required. First, the reference profiles of potential density $\overline{\sigma_0}(z)$, temperature $\overline{T}(z)$, and salinity $\overline{S}(z)$ are computed using the previous part, concatenating the Argo float data. Thermohaline anomalies on isopycnals $\Delta_{\sigma_0}T$ and $\Delta_{\sigma_0}S$ can thus be calculated using equations (1) and (2). These anomalies are calculated at isopycnal levels. Second, $\hat{T}(x,z)$ and $\hat{S}(x,z)$ are obtained according to equations (3) and (4) by interpolating these anomalies on geopoten-

tial levels. Then, using the equation of state for seawater (TEOS-10 standard), $\hat{\sigma_0}(x,z)$ is obtained and subtracted from $\sigma_0(x,z)$, the *in situ* potential density. This subtraction must be performed at geopotential levels. According to equation (8), the quantity obtained is $\delta^2\sigma_0(x,z)$. Finally, according to equation (11), $\overline{\sigma_0}(z)$ is subtracted from $\hat{\sigma_0}(x,z)$ to obtain $\delta\sigma_0(x,z)$. This subtraction must also be performed at geopotential levels. Then $\delta\sigma_0(x,z)$ has to be divided by the vertical gradient of $\overline{\sigma}$, which sometimes causes overshoots due to spurious points. Some of them will be removed.

Then, after separating the variables, we can write

$$\sigma_0(x,z) = \overline{\sigma_0}(z) - \phi(x)\psi(z)\frac{d\overline{\sigma_0}}{dz} + \chi(x)\xi(z) \tag{37}$$

with,

$$\phi(x) = \exp\left(-\left(\frac{x-x_1}{R_1}\right)^{\alpha_1}\right) \tag{38}$$

$$\chi(x) = \exp\left(-\left(\frac{x-x_2}{R_2}\right)^{\alpha_2}\right) \tag{39}$$

where x_1 and x_2 are the location of the maximum on the ship track for ϕ and χ respectively. We will refer to this function as "alpha-exponential". And ψ, ξ are defined by equations (34) and (35). While studying the data, we noticed that there was an offset for both ψ and ξ. So both functions are shifted by a constant. Therefore, we introduce B and D so that:

$$\psi(z) = \psi_0\left(\frac{z-z_1}{H_1}\right)\exp\left(-\frac{(z-z_1)^2}{H_1^2}\right) + B \tag{40}$$

$$\xi(z) = \xi_0\exp\left(-\frac{(z-z_2)^2}{H_2^2}\right) + D \tag{41}$$

The origin of these offsets will be discussed later, but we can interpret them as a small correction that does not change the shape of the anomaly. For each eddy, these generic expressions are fitted to the data using the nonlinear least squares algorithm scipy.optimize.curve_fit in Python to determine z_1, H_1, ψ_0, z_2, H_2, ξ_0, x_1, R_1, α_1, x_2, R_2, α_2, B, and D by minimizing the root mean square (RMS).

Since we have analyzed full vertical sections of the eddies, we consider only even functions with respect to the eddy center. Consequently, α_1 and α_2 are assumed to be even as if the eddy was axisymmetric. For odd values, an exponential-alpha function diverges for x tending to $-\infty$. For ψ and ξ, the optimization is performed at the eddy center, i.e. at the location where the isopycnal deviation is maximum (where $\delta\sigma_0$ is maximum). For ϕ and χ the optimization is performed at the location where the amplitudes of ψ and ξ are maximum, respectively. Therefore, vertical optimizations are performed before horizontal optimizations. Finally, to evaluate the relevance of the proposed expressions, the Root Mean Squared (RMS) between the data and the theoretical predictions is computed at the end of the optimization.

4 Results

4.1 First case study: Potential density decomposition for the subsurface AE sampled during EUREC4A-OA

In this section, the previously developed methodology of potential density field decomposition is applied. The approach has obviously been applied to all other eddies, but for the sake of clarity we present only two cases: one is the subsurface intensified AE sampled during the EUREC4A-OA experiment (this section), and the other is the surface intensified AE sampled during the PHYSIDIEN 2011 experiment (next part). The total smoothed *in situ* fields are plotted in figure 4 panels (a) and (d). The associated potential density σ_0 is also calculated and the isopycnals are plotted as dark lines. The separation of the latter (see isopycnals of values $26.5kg/m^3$ and $27kg/m^3$) in the vortex core characterizes the anticyclonic nature of the considered structure.

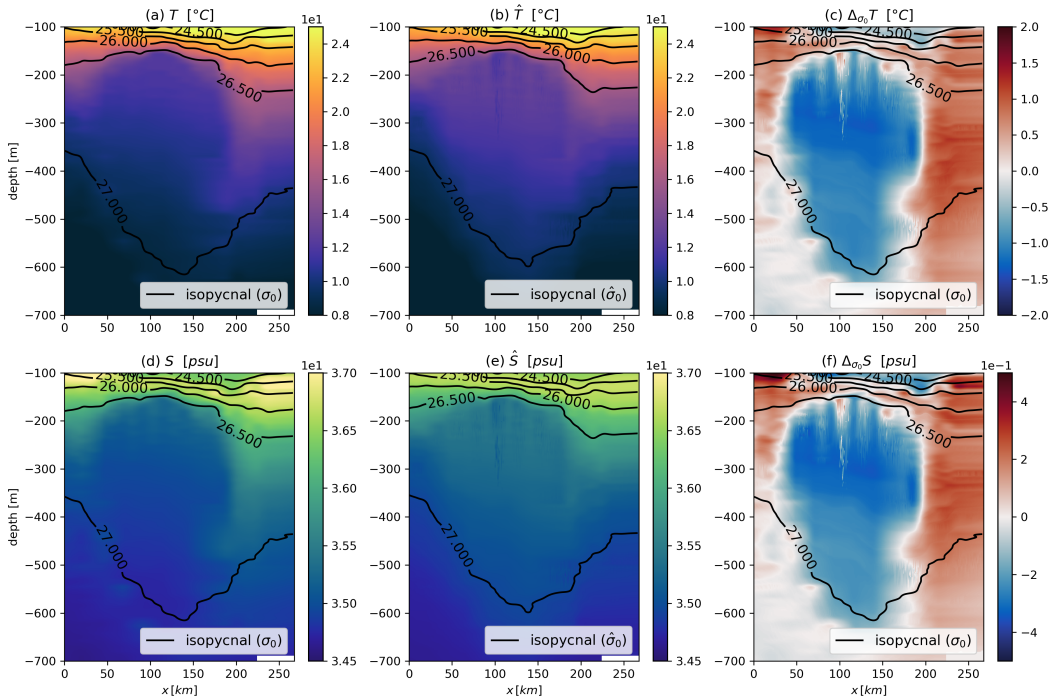

Figure 4. 2D vertical sections across the subsurface eddy core obtained from EUREC^{4}A-OA data. For each panel, the horizontal axis is the horizontal scale in kilometers and the vertical axis is the depth in meters. Isopycnals are shown as dark lines. (a) is the smoothed *in situ* temperature field. (b) is the modified *in situ* temperature $\hat{T}$ field without the thermal anomaly on isopycnals. (c) is the isopycnal thermal anomaly interpolated to geopotential level. (d) is the smoothed *in situ* salinity field. (e) is the modified *in situ* salinity $\hat{S}$ field without the salinity anomaly on isopycnals. (f) is the salinity anomaly on isopycnals interpolated to geopotential level. Note that isopycnals are plotted with the $\hat{\sigma_0}_0$ density field for panels (b) and (e).

Thermohaline anomalies on isopycnals are then calculated and interpolated to geopotential levels. Vertical sections are shown in figure 4(c), (f). The core of this anticyclonic eddy shows a significant negative anomaly in temperature and salinity: a colder but less salty water mass is trapped (relative to the surrounding water). The temperature and salinity anomalies reach values of the order of $-1.6°C$ and $-0.3psu$ in the eddy core. The moduli of the anomalies are maximum in the center and quite homogeneous. They de-

crease very rapidly at the eddy boundary, where the trapped water meets the surrounding water. Note also that the anomalies decrease slightly with depth because the water masses tend to homogenize with depth.

These anomalies are then removed from the total *in situ* thermohaline fields to compute $\hat{T}/\hat{S}$ fields as if the trapped water mass had the same thermohaline properties as the surrounding water. Associated vertical sections are shown in figure 4 (b), (e). The associated potential density $\hat{\sigma_0}$ is also calculated and isopycnals are plotted as dark lines. These isopycnals are similar to those of the σ_0 field. However, small variations can be observed after isopycnals of $26.5kg/m^3$ and $27kg/m^3$, showing that the trapped water properties have a direct influence on the density field. When the thermohaline anomalies on isopycnals are removed from the entire T/S fields, the core appears to be warmer and more saline, which is consistent with the sign of these anomalies.

Figure 5 shows the potential density decomposition for the anticyclonic eddy that was sampled during the EUREC^{4}A-OA experiment. The fourth quantities of interest are plotted: the potential density σ_0 computed with *in situ* T/S fields (panel (a)), the potential density $\hat{\sigma_0}$ computed with modified $\hat{T}/\hat{S}$ fields (panel (b)), the first potential density anomaly $\delta\sigma_0$ representing the deviation of isopycnals without the effect of trapped water (panel (c)), and the second potential density anomaly $\delta^2\sigma_0$ illustrating the effect of thermohaline anomalies on isopycnals (panel (d)).

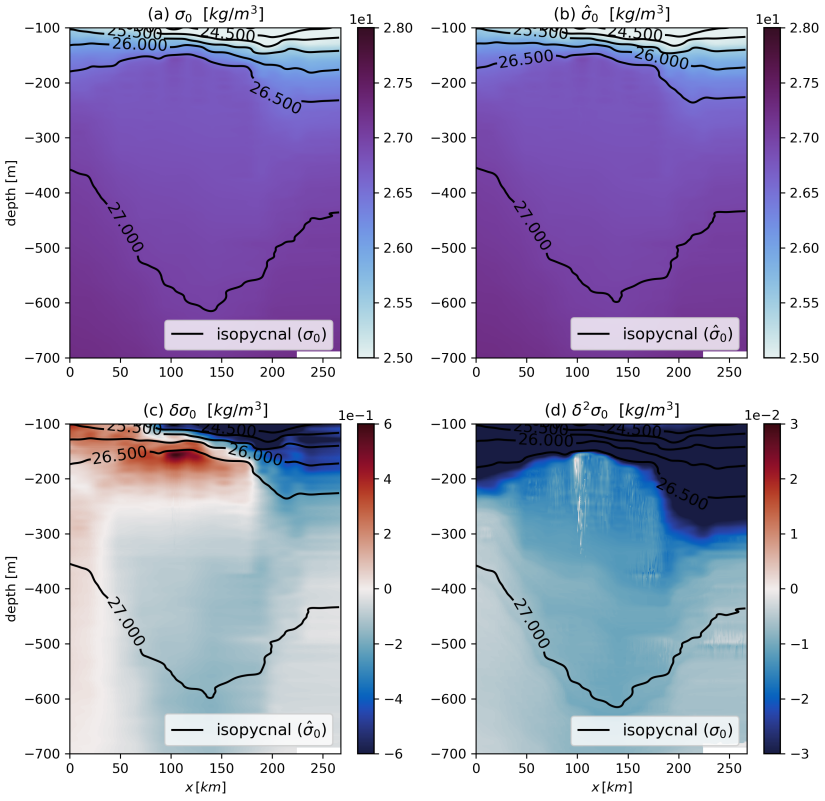

Figure 5. Density decomposition in the eddy core from EUREC^{4}A-OA data. Axis are the same as in Fig.4. (a) represents the total potential density field computed from the T/S fields. (b) is the modified potential density field computed using $\hat{T}/\hat{S}$ fields. (c) is the deviation of the isopycnals computed using equation (11). (d) is the contribution of the trapped water mass properties computed using equation (8).

As mentioned in section 4.1, the σ_0 and $\hat{\sigma_0}$ fields are similar: the amplitudes are relatively similar and the isopycnal deviation is reasonably conserved when passing from one field to the other. In fact, as shown in panel (d), the density anomaly component associated with the difference in water masses between the core and the environment reaches only very small values of the order of $-0.015 kg/m^3$ in the core. This field is also smaller than that of the isopycnal anomaly $\delta\sigma_0$ in panel (c). Indeed, the latter reaches values of the order of $0.5 kg/m^3$ in the eddy core, which is four times that of $\delta^2\sigma_0$. This is also in agreement with the theoretical results. Note that the $\delta\sigma_0$ field changes sign at about 250 m depth, which is consistent with the spacing of isopycnals in an anticyclonic eddy: isopycnals in the upper part of the core are shallower and those in the lower part of the core are deeper than the surrounding environment. In summary, in orders of magnitude, the isopycnal deviation is the largest contributor to the total potential density anomaly.

As mentioned before, the small amplitude of $\delta^2\sigma_0$ can be explained by a gravitational argument. Indeed, considering this materially coherent eddy as a closed system, the eddy domain tends to be in hydrostatic equilibrium with the surrounding water. The effect of the temperature anomaly on the isopycnals is almost compensated by that of the salinity anomaly on the isopycnals, so that the hydrostatic equilibrium is verified (denser water remains below lighter water). Therefore, the modulus $\delta^2\sigma_0$ in the eddy core is larger than in the surrounding water below 300 m depth, but smaller than in the surrounding water above 300 m depth (see panel (d)). This can be seen in panel (d), where the color above the eddy core is much darker than the color below the eddy core. This effect creates a horizontal buoyancy gradient and thus a velocity component due to the thermal wind effect.

4.2 Second Case Study: Potential density decomposition for the surface AE sampled during PHYSINDIEN 2011

Similar to figure 4, figure 6 presents results for the anticyclonic eddy sampled during the Physindien 2011 experiment: Panels (a) and (b) show the smoothed *in situ* thermohaline fields, panels (b) and (e) show the modified thermohaline fields when the thermohaline anomalies on isopycnals have been removed, and panels (c) and (f) show the thermohaline anomalies on isopycnals interpolated to geopotential levels.

This anticyclonic eddy shows a positive anomaly for both temperature and salinity fields: a warmer and saltier water mass is trapped in the eddy core. The anomalies reach values of the order of $0.6°C$ and $0.1 psu$. Although this anticyclonic eddy appears to be of surface type, its anomaly maximum is located at a depth of about $70m$ for both thermal and salinity fields. As a consequence, the altimetric data would not have been able to detect the real signature of this warm core by looking only at the surface fields. The 2D vertical section also shows second positive extrema for both thermal and haline anomalies at $-250m$ depth. Between $-70m$ and $-250m$ both anomalies decrease to a minimum at about $-150m$ depth. This core is surrounded by a crown of colder and fresher water as characterized by the negative anomaly around $x = 400km$ and $x = 550km$ in panels (c) and (f).

Constructed $\hat{T}/\hat{S}$ fields show noticeable differences from the real T/S fields. The global structure of the eddy appears colder and less salty without thermohaline anomalies on isopycnals, consistent with their signs. The shape of the isopycnals is also affected. For example, the $24 kg/m^3$ isopycnal appears deeper with $\hat{T}/\hat{S}$ fields. On the contrary, the isopycnal of value $25.5 kg/m^3$ appears shallower with $\hat{T}/\hat{S}$ fields.

Similar to figure 5, figure 7 shows the potential density decomposition. The panels are presented in the same order as before. Basically, the same remarks can be made for this anticyclonic vortex.

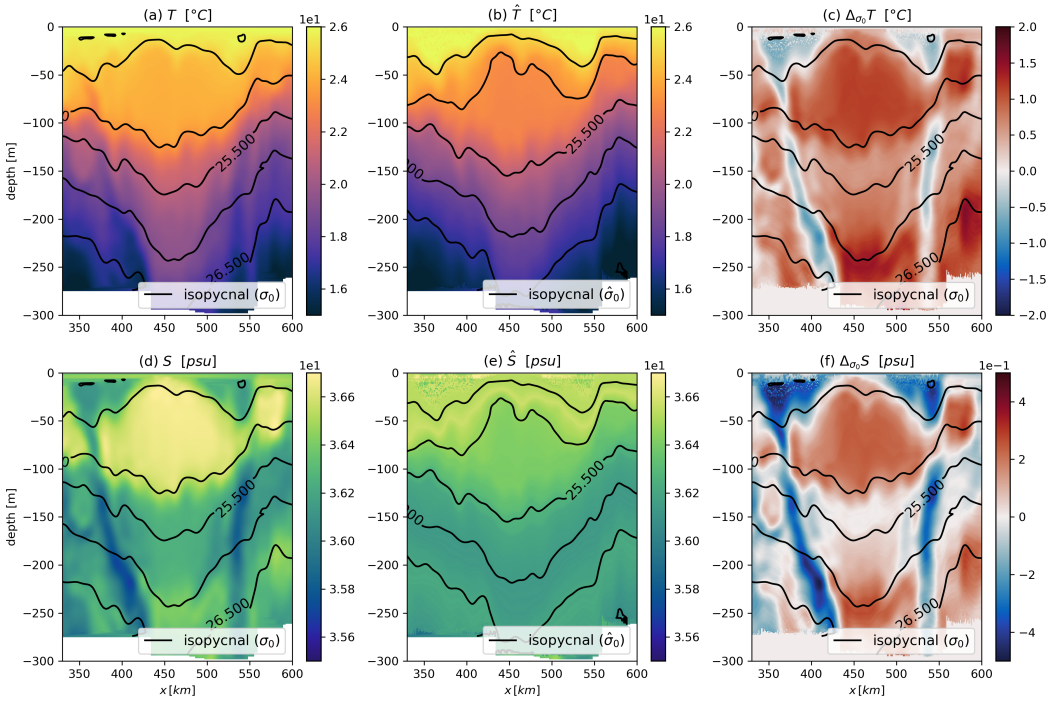

Figure 6. 2D vertical sections across the eddy core from the 2011 Physindien data. For each panel, the horizontal axis is the horizontal scale in kilometers and the vertical axis is the depth in meters. Isopycnals are shown as dark lines. (a) is the smoothed *in situ* temperature field. (b) is the modified *in situ* temperature $\hat{T}$ field without the thermal anomaly on the isopycnal. (c) is the isopycnal thermal anomaly interpolated to geopotential levels. (d) is the smoothed *in situ* salinity field. (e) is the modified *in situ* salinity $\hat{S}$ field without the salinity anomaly on isopycnals. (f) is the salinity anomaly on isopycnals interpolated to geopotential level. Note that for panels (b) and (e) the isopycnals are plotted with the $\hat{\sigma}_0$ density field.

Panels (a) and (b) illustrate the similarity between σ_0 and $\hat{\sigma}_0$, although small differences are noticeable. In particular, there are differences between $-50m$ and $-100m$ depth, which is the location of the warm wear. Panel (c) shows that the density anomaly associated with the isopycnal anomaly reaches values of the order of $0.4kg/m^3$, while panel (d) shows a rather constant density anomaly of the order of $-0.15kg/m^3$. In terms of $\delta\sigma_0$, $\delta^2\sigma_0$ is larger for this anticyclonic eddy than for the one from the EUREC^{4}A-OA experiment. However, the variations of this field are much more smaller in the case of the eddy from Physindien 2011.

In this case, we can expect the horizontal gradient of $\delta^2\sigma_0$ to be smaller than that of $\delta\sigma_0$. The velocity field produced by the trapped water mass properties will then be smaller than that produced by the isopycnal anomaly.

4.2.1 Shape of the potential density field in the eddy core

4.2.2 Vertical extent of $\delta\sigma_0$

After decomposing the potential density field for each eddy, we first study the vertical shape of $\delta\sigma_0$, which we defined as ψ in the theoretical part. The results are shown in figure 8. The values of the optimized parameters are written above each panel.

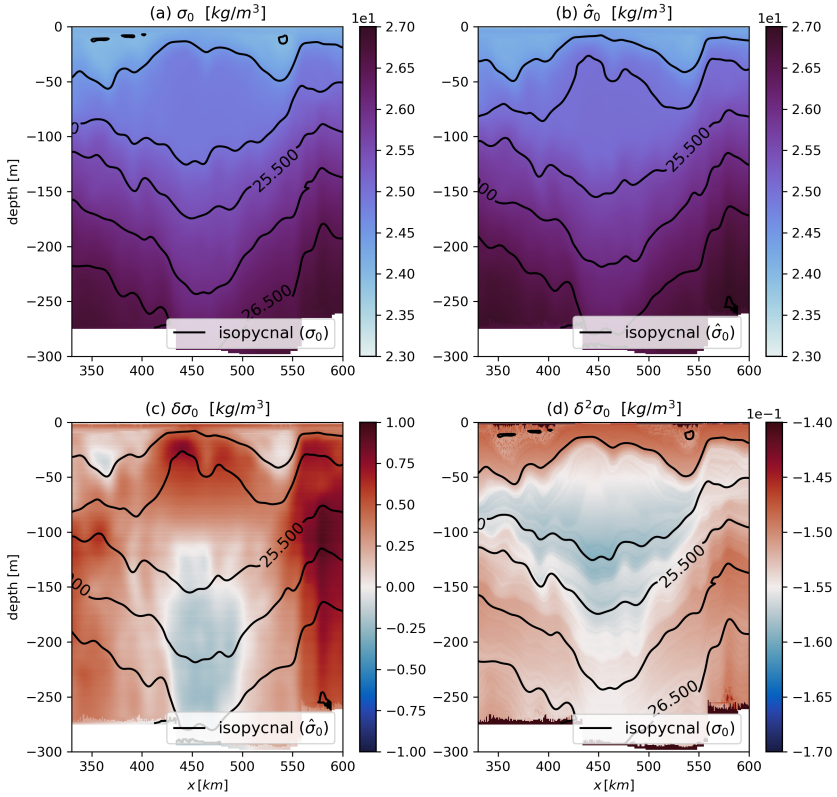

Figure 7. Density decomposition in the eddy core from Physindien 2011 data. Axis are the same as in Fig.6. (a) represents the total potential density field computed using the T/S fields. (b) is the modified potential density field computed using $\hat{T}/\hat{S}$ fields. (c) is the deviation of the isopycnals computed using equation (11). (d) is the contribution of the trapped water mass properties computed using equation (8).

Panel (a) is dedicated to the surface AE sampled during the EUREC^{4}A-OA cruise. Due to noise points near the surface, the shallower point is set to $-30m$. We extend the optimization far below the point of maximum velocity, which is about $-50m$ for this eddy. Since this eddy is at the surface, we could only fit the part when ψ is negative. This corresponds to the region where isopycnals dive to create a horizontal density gradient. Thus, ψ is linear from $-30m$ to $-100m$ and undergoes a Gaussian decay below that. The theoretical prediction is reasonable with an RMS of 5.52% of the total signal amplitude.

Panel (b) is dedicated to the subsurface AE sampled during the EUREC^{4}A-OA cruise. According to Figure 2 panels (a) and (e), this AE was sampled very close to the previous surface AE and in a very short period of time. As a result, the density anomaly on the shallower part of the subsurface AE is influenced by that of the surface AE. In Figure 3 panel (b), for $z \in [-200m; -140m]$ and $x \in [0km; 100km]$, we can easily guess the presence of the subsurface structure. Indeed, if we look closely at the density values, we see that the left part of the section below $-140m$ is denser than the right part; this density value on the right is the same as that of the core of the subsurface structure shown in panel (a). As a result, the difficulty in determining ψ was to choose the relevant depth threshold so as to accurately model the structure of the subsurface structure rather than that of the surface structure. Therefore, after optimization, the theoretical model agrees well with the data with an RMS value of 8% of the total amplitude

and predicts a median plane of the eddy located at $-343m$, which is consistent with figure 3 panel (a).

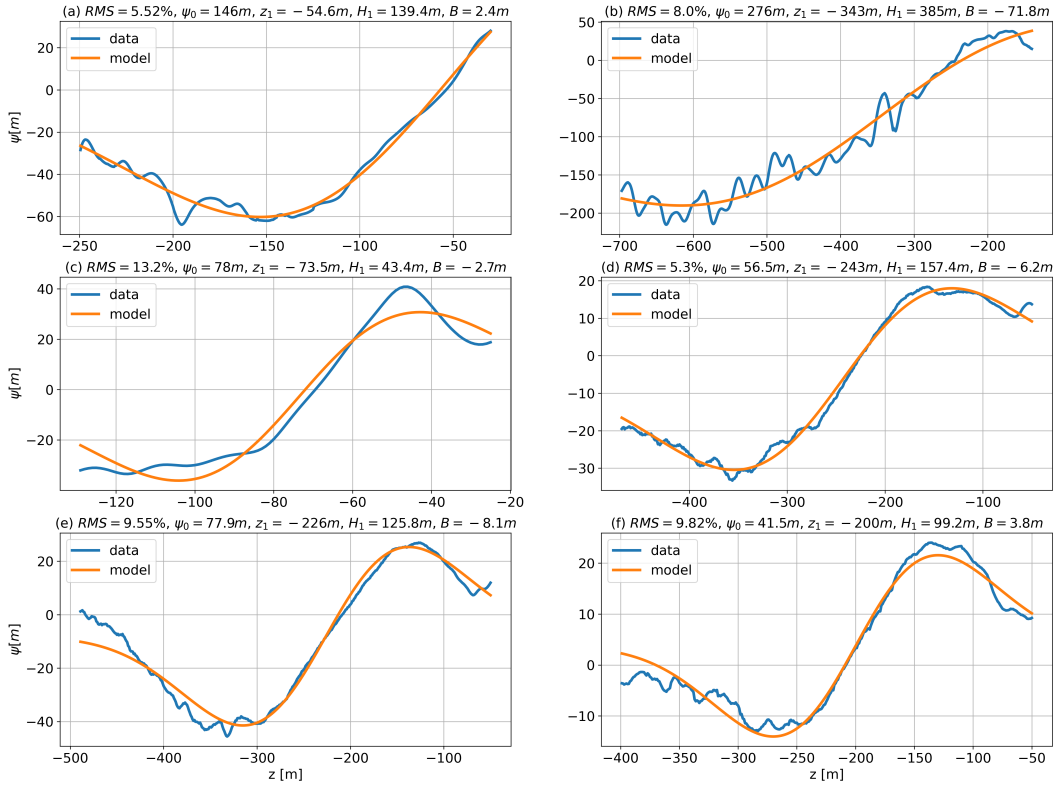

Figure 8. Comparison between data and the theoretical prediction for $\psi(z)$. For each panel, the horizontal axis is the depth in $[m]$ and values of optimized parameters are written above each panel. The blue (resp. orange) curve represents the data (resp. the theoretical prediction optimized by the non-linear least squares algorithm). (a) surface AE from EUREC^{4}A-OA data. (b) subsurface AE from EUREC^{4}A-OA data. (c) surface AE from PHYSINDIEN 2011 data. (d), (e) and (f) AEs sampled during M124 cruise.

Panel (c) is dedicated to the surface AE sampled during the PHYSINDIEN 2011 experiment. Although the maximum velocity is reached at the surface, the median plane seems to be between $-50m$ and $-100m$ according to figure 3 panel (c). The shape is also different from the others. As a result, the theoretical prediction for ψ agrees with the data only with an RMS value of 13.2% of the maximum amplitude. However, we recover that the median plane is located at $-73.5m$ with a linear behavior of ψ around this value and an exponential damping. Even with filtering, overshoots were found deeper than $-120m$, so we truncated the fit accordingly.

Panels (d), (e), (f) are dedicated to the three AEs sampled during the METEOR 124 experiment. As mentioned before, these eddies have an imprint on the sea surface height, but their cores are clearly located below the pycnocline according to Figure 3 panels (d), (e), (f). This observation underlines the fact that the study of eddies using satellite altimetry alone is not sufficient to properly quantify their influence on tracer transport (see (Barabinot et al., 2023) for more details). For these three structures, the theoretical prediction works reasonably well, with RMS less than 10% of the maximal signal amplitude.

It is important to note that vertical levels of *in situ* data collected by ships are vertically limited. Therefore, the panels of the figure 8 are limited. In addition, the resolution of *in situ* data is often higher near the surface. When interpolating and filtering, eddy structures can be distorted, especially in their deeper part. This may explain why the theoretical predictions in panels (e) and (f) do not seem to fit the data well at depth. Overall, ψ seems to describe the vertical structure of these eddies well.

4.2.3 Horizontal extent of $\delta\sigma_0$

After decomposing the potential density field for each eddy and analyzing the vertical extension ψ, we now study the horizontal shape of $\delta\sigma_0$, which we defined as ϕ in the theoretical part. The results are shown in figure 9. The panels are presented in the same order as in figure 8.

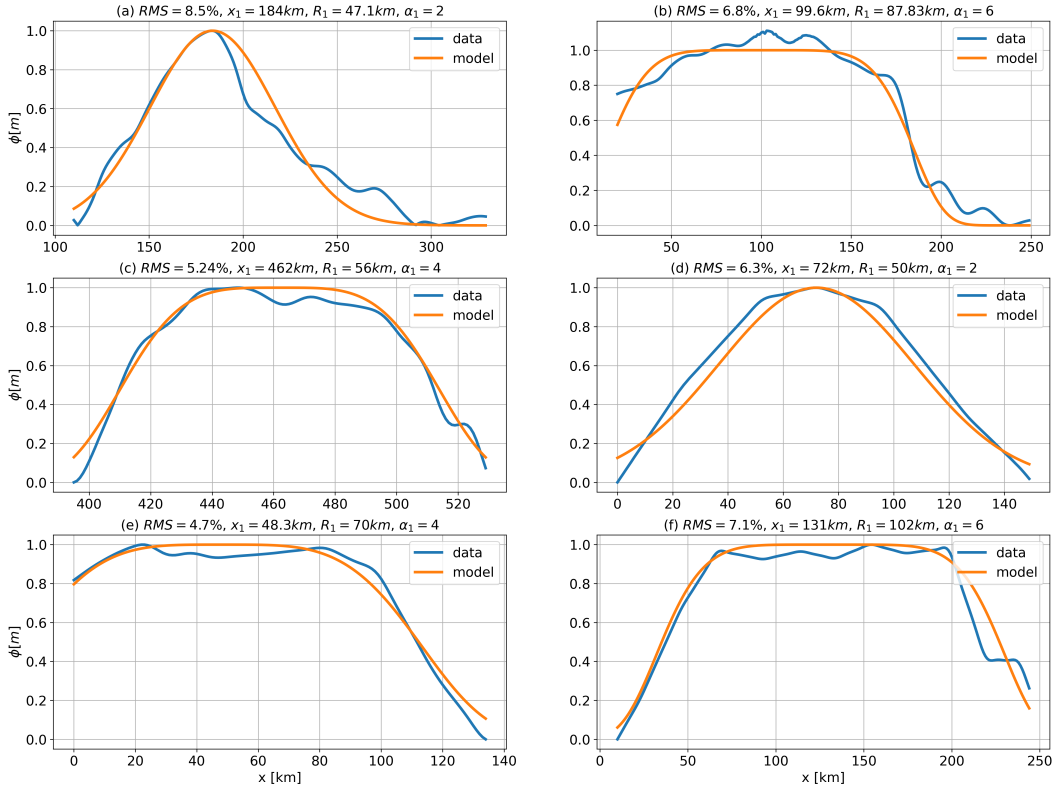

Figure 9. Comparison between data and theoretical prediction for $\phi(x)$. For each panel, the horizontal axis is the horizontal transect in $[km]$. The blue (respectively orange) curve represents the data (respectively the theoretical prediction optimized by the nonlinear least squares algorithm). (a) Surface intensified AE from EUREC^{4}A-OA data. (b) Subsurface intensified AE from EUREC^{4}A-OA data. (c) Surface intensified AE from PHYSINDIEN 2011 data. (d), (e) and (f) AEs sampled during the M124 cruise.

For each panel, the theoretical prediction using an alpha exponential shape matches the form of ϕ. In each case, the RMS is less than 10% of the maximum amplitude, which is unity here. However, contrary to previous studies on the subject, the value of α_1 can reach higher values than 2, which is the reference for Gaussian eddies. This parameter is important because it controls the value of the horizontal gradient of $\delta\sigma$ and thus the velocity field. The higher the value of α_1, the higher the horizontal gradient and the higher

the velocity maximum. Of the 6 eddies, only 2 were optimized as Gaussian eddies (panels (a) and (d)). For the 4 others, the anomaly is nearly constant in the core and decreases very rapidly at the eddy boundary. For example, in panel (e), ϕ is close to 1 for $x \in [20km; 80km]$, but decreases very rapidly outside this region with $\alpha_1 = 4$. Similarly, in panel (f), ϕ is close to 1 for $x \in [60km; 200km]$, but decreases very quickly out of this region with $\alpha_1 = 6$. In 2D, these density profiles may induce some barotropic instabilities (Carton & McWilliams, 1989), the stratification helps to stabilize the flow.

Gaussian shapes are self-similar solutions associated with diffusive processes. The well-known Lamb-Oseen vortex for incompressible and unsteady flow is an example (Oseen, 1912). In the global ocean, however, mesoscale eddies are rarely, if ever, completely isolated. Consequently, their boundaries are subject not only to diffusion, but also to advection and shear from the background flow. The external flow thus has the ability to erode the rotating flow and increase the steepness of the velocity profile (modeled here by the parameter α_1). In this case, the vortex diffuses less momentum into the background flow (Legras & Dritschel, 1993; Mariotti et al., 1994).

4.2.4 Vertical extent of $\delta^2\sigma_0$

After looking at $\delta\sigma_0$, we analyze the vertical expansion of $\delta^2\sigma_0$. We recall that this term results from the presence of another water mass in the eddy core. We proposed a Gaussian shape to model it. The results are shown in Figure 10. The panels are presented in the same order as in figure 8.

For each panel, the anomaly presents a unique extremum that decreases exponentially with depth. However, panels (b), (d), (e) and (f) show that the behavior near the surface is barely captured by the Gaussian. The signal is therefore not symmetrical. Moreover, the extremum is often located either above the median plane (see panels (b), (d), (e), (f)) or below it (see panels (a) and (c)). For example, in panel (b) the minimum of ξ is reached at a depth of $-254m$, while the median plane determined by ψ was around $-343m$. The same can be said for panels (e), (f) and (g), where the maxima of ξ are found around $-100m$ depth, while the median planes were found deeper using ψ around $-220m$. It is difficult to detect a clear minimum for panel (c) due to some overshoots below $-120m$, but the signal decreases below the median plane found using ψ. Similarly, the minimum in panel (a) is reached around $-175m$, which is below the median plane of ψ.

In any case, looking at the RMS values, the Gaussian shape seems to be a relevant representation of this quantity ξ, even if some imperfections can be found near the surface. One hypothesis could be that the high variability of water properties near the surface due to atmospheric forcing influences both the local stratification and the heat and salt content in the eddy core (which in practice is quantified by anomalies calculated on isopycnals, see Eqs. (1) and (2)). Temperature and salinity can diffuse faster clause to the surface, causing $\delta\sigma_0$ to change faster. This results in these non-symmetric Gaussian shapes.

4.2.5 Horizontal extent of $\delta^2\sigma_0$

Finally, we analyze the horizontal extension of $\delta\sigma_0$, which we called χ in the theoretical part. The results are shown in Figure 11. The panels are presented in the same order as in Figure 8.

It is important to note that the shapes are similar to those in Figure 9. The values of the parameters R_2, x_2 and α_2 are very similar to the values of the parameters R_1, x_1 and α_1 that were found to model ϕ. For example, taking panel (b) as an example, we previously found $R_1 = 87.8km$, $x_1 = 99.6km$, and $\alpha_1 = 6$ in figure 9. Here $R_2 = 85.2km$, $x_2 = 98.4km$ and $\alpha_2 = 6$ were found.

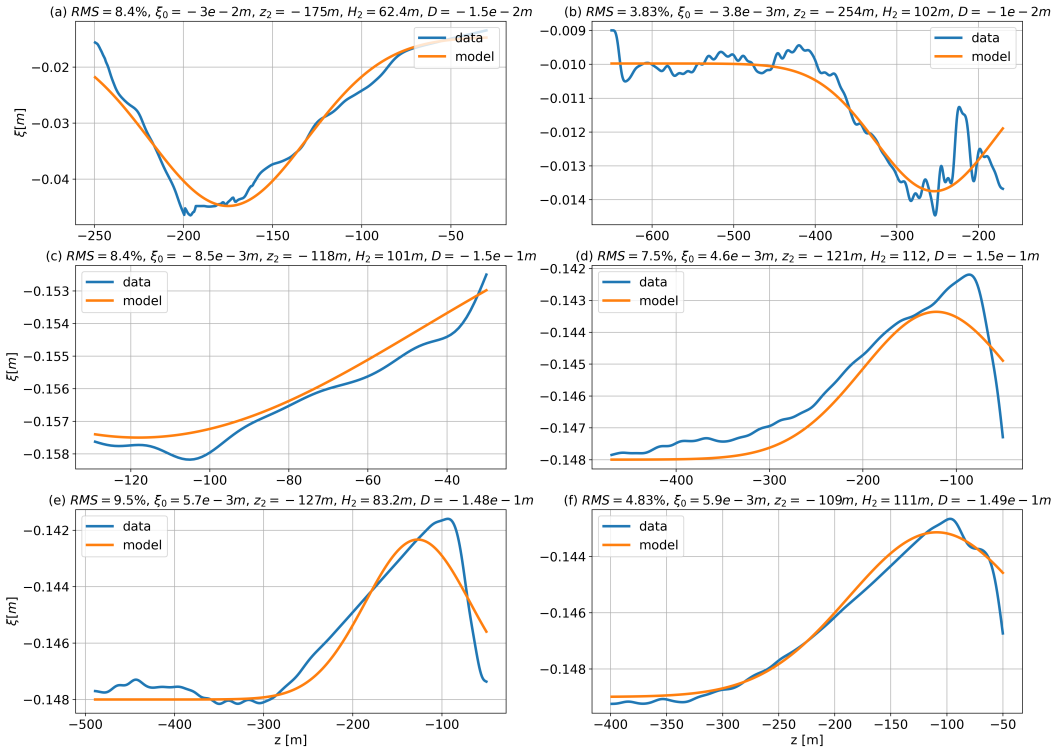

Figure 10. Comparison between the data and the theoretical prediction for $\xi(z)$. For each panel, the x axis is the depth in $[m]$. The blue (respectively orange) curve represents the data (respectively the theoretical prediction optimized by the nonlinear least squares algorithm). (a) Surface intensified AE from EUREC^{4}A-OA data. (b) Subsurface intensified AE from EUREC^{4}A-OA data. (c) Surface intensified AE from PHYSINDIEN 2011 data. (d), (e) and (f) AEs sampled during the M124 cruise.

As for ϕ, the anomaly is relatively constant in the core and decreases rapidly at the edge of the eddy. The higher the α_2, the higher the horizontal gradient of $\delta^2\sigma_0$. For example, on panel (e), χ is close to 1 for $x \in [20km; 80km]$, but decreases very rapidly outside this region with $\alpha_2 = 4$. Similarly, on panel (f), ϕ is close to 1 for $x \in [60km; 200km]$, but decreases very sharply out of this region with $\alpha_2 = 6$.

Looking at the RMS values, we can say that the alpha exponential function is appropriate for predicting the horizontal variation of $\delta\sigma_0$.

5 Discussion

5.1 3D Reconstruction

From the previous results, the overall expression of the density anomaly can be simplified. First of all, as shown in Figures 4 and 6, $\delta^2\sigma_0$ is a very small quantity compared to $\delta\sigma_0$. They differ by one or two orders of magnitude depending on the eddy. Furthermore, if we look carefully at x_1, R_1, α_1, x_2, R_2, α_2, their horizontal extent remains very similar. In this case, the radial variations of $\delta\sigma_0$ are much more important than those of $\delta^2\sigma_0$. Therefore, first, $\delta\sigma_0$ is the main driver of the rotating flow by the thermal wind balance, and second, $\delta^2\sigma_0$ can be neglected to reconstruct the density structure of mesoscale eddies and to study their dynamics.

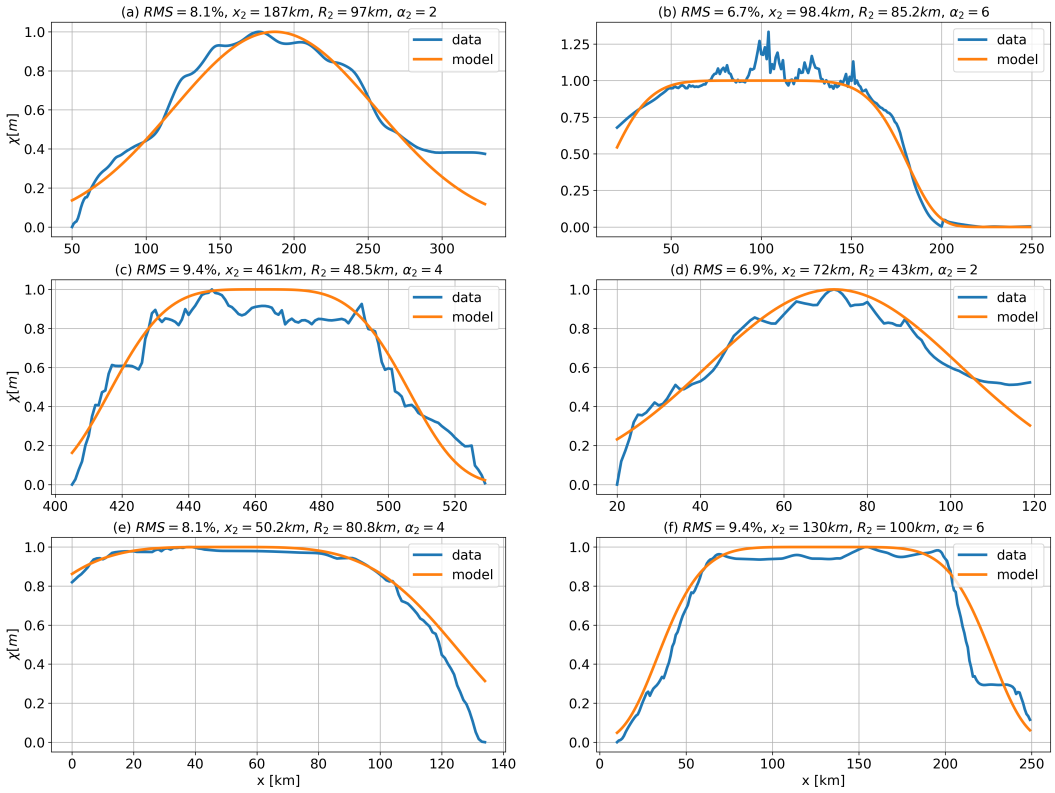

Figure 11. Comparison between data and theoretical prediction for $\chi(x)$. For each panel, the horizontal axis is the horizontal transect in $[km]$. The blue (or orange) curve represents the data (or the theoretical prediction optimised by the nonlinear least squares algorithm). (a) Surface intensified AE from EUREC^{4}A-OA data. (b) Surface intensified AE from EUREC^{4}A-OA data. (c) Surface intensified AE from PHYSINDIEN 2011 data. (d), (e) and (f) AE sampled during the M124 cruise.

Moreover, B is much smaller than ψ_0 in the vertical extension of $\delta\sigma_0$, except for the subsurface intensified eddy sampled during EUREC^{4}A-OA. A suggestion is therefore to neglect this offset in the overall formula. Note that, as mentioned above, the said subsurface intensified AE lies below the surface intensified AE of 3 panel (b), which may flatten the isopycnals and thus increase the vertical asymmetry of $\psi(z)$.

These considerations lead to a simplified but accurate formula for the density field:

$$\sigma_0(x,z) = \overline{\sigma_0}(z) - \psi_0 \frac{d\overline{\sigma_0}}{dz}\left(\frac{z-z_1}{H_1}\right)\exp\left(-\left(\frac{z-z_1}{H_1}\right)^2 - \left(\frac{x-x_1}{R_1}\right)^{\alpha_1}\right) \tag{42}$$

As an example, we show in Figure 12 the reconstructed field of the surface intensified AE sampled during EUREC^{4}A-OA and compare it with the *in situ* field. It is clear that the extent of the anomaly is correctly reconstructed.

5.2 Link between vertical sections and 3D structure

According to what has been shown, mesoscale eddies sampled on 2D vertical sections are well modelled, separating their density anomaly into 2 parts: one driven by the

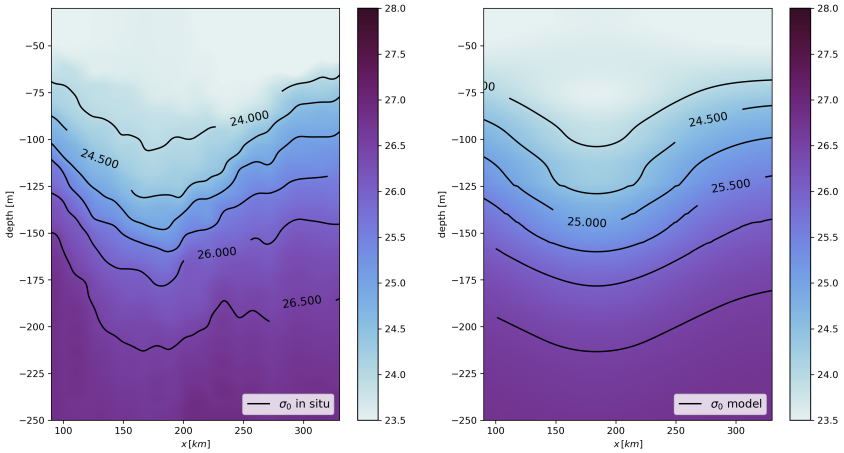

Figure 12. Right : *in situ* potential density field; left : reconstructed potential density field

isopycnal deviation and the other by the trapped water properties within the eddy core. However, at first it is difficult to infer the 3D structure of the eddies, especially their horizontal extent, by looking only at 2D vertical sections. The 2D horizontal reconstruction can only be an extrapolation of the 2D vertical sections with some assumptions. In this section we discuss the correspondence between the model on the 2D vertical section and that in the 3D cylindrical frame.

Assuming that the eddy is axisymmetric and that the ship track passes perfectly through the centre of the eddy, the variable r is equivalent to the variable x. In this case the horizontal functions ϕ and χ correspond perfectly. However, if the eddy is not axisymmetric, as is often the case (Chen et al., 2019), nothing can be said about the variable θ. In particular, it is almost impossible to reconstruct $\varepsilon(\theta)$ and $\beta(\theta)$ from just one ship track.

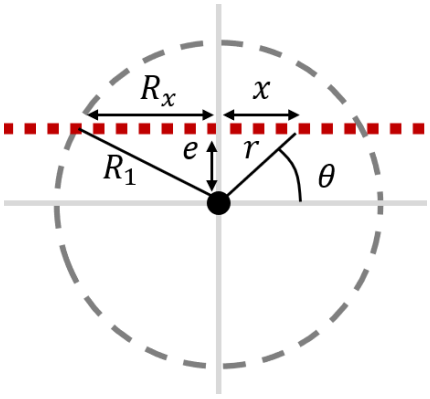

Figure 13. Sketch showing the track of a ship (red squares) crossing an axisymmetric eddy of radius R_1 with a small displacement e. The radius of the eddy appears as $R_x < R_1$ on the vertical section.

In practice, this perfect section rarely passes through the centre of the eddy and we often have a small shift (called e in the figure 13). Therefore, the variable x does not always correspond to r. The point is therefore to understand the effect of this small shift

on what we observe on 2D vertical sections. On the vertical, the shape of the anomaly remains the same whatever the shift. In fact, at the centre, the anomalies have their maximum amplitude, which decreases as we move away from the centre, but the shape remains the same. In fact, this shift will mainly affect the horizontal functions ϕ and χ. Using the figure 13, we try to relate the horizontal function in 3D, ϕ_r (or χ_r), and the horizontal function in the 2D vertical section, ϕ_x (or χ_x). The aim is to quantify the error between these 2 functions when an eddy has been sampled. For simplicity, the eddy is assumed to be axisymmetric, although this is not always verified in practice. Considering any other type of shape would lead to a coupling between the variables r and θ (as for an elliptical shape) and the calculations would be complicated. The idea here is to find orders of magnitude.

Let us start with ϕ_r. This function obviously writes:

$$\phi_r(r) = \exp\left(-\left(\frac{r}{R_1}\right)^{\alpha_1}\right) \tag{43}$$

with $r^2 = x^2 + e^2$ and $R^2 = R_x^2 + e^2$, we write:

$$\phi_r(x) = \exp\left(-\left(\frac{x^2+e^2}{R_x^2+e^2}\right)^{\alpha_1/2}\right) \tag{44}$$

In comparison, ϕ_x writes:

$$\phi_x(x) = \exp\left(-\left(\frac{x}{R_x}\right)^{\alpha_1}\right) \tag{45}$$

Note that we consider that $x_1 = 0$ on the vertical section and that α_1 is not modified, which is a property of exponential-alpha functions: any section by a plane parallel to the z axis, will give an exponential-alpha function. As a simple example, the 3D surface $z = \exp(-x^2 - y^2)$ cut by the plane $x = 0$ gives the Gaussian $z = \exp(-y^2)$ and α is not modified.

Let us start with the case $x \approx 0 \Leftrightarrow r \approx e$. In this case we have

$$\phi_r(e) = \exp\left(-\left(\frac{e^2}{R_x^2+e^2}\right)^{\alpha_1/2}\right) \tag{46}$$

which can be written:

$$\phi_r(e) = \exp\left(-\left(\frac{e}{R_x}\right)^{\alpha_1}\left(\frac{1}{1+(e/R_x)^2}\right)^{\alpha_1/2}\right) \tag{47}$$

Assuming that e/R_x is much smaller than the unity, we use a Taylor expansion. After some calculations, we end up with:

$$\phi_r(e) = \phi_x(e)\left(1 + \frac{\alpha_1}{2}\left(\frac{e}{R_x}\right)^{\alpha_1+2} + O\left(\frac{\alpha_1}{2}\left(\frac{e}{R_x}\right)^{\alpha_1+2}\right)\right) \tag{48}$$

The second case is when $x \approx e \Leftrightarrow r \approx \sqrt{2}e$. Therefore, we write:

$$\phi_r(\sqrt{2}e) \approx \exp\left(-\left(\frac{2e^2}{R_x^2+e^2}\right)^{\alpha_1/2}\right) \tag{49}$$

Using the same technique as before, we Taylor expend in power of e/R_x. It leads to:

$$\phi_r(\sqrt{2}e) = \phi_x(\sqrt{2}e)\left(1+(\sqrt{2})^{\alpha_1}\frac{\alpha_1}{2}\left(\frac{e}{R_x}\right)^{\alpha_1+2}+O\left((\sqrt{2})^{\alpha_1}\frac{\alpha_1}{2}\left(\frac{e}{R_x}\right)^{\alpha_1+2}\right)\right) \tag{50}$$

Finally, for $x \gg e \Leftrightarrow r \approx x$, we can write:

$$\phi_r(x) \approx \exp\left(-\left(\frac{x^2}{R_x^2+e^2}\right)^{\alpha_1/2}\right) \tag{51}$$

Assuming that x cannot be much larger than R_x, after the Taylor expansion, we end up with:

$$\phi_r(x) = \phi_x(x)\left(1+\frac{\alpha_1}{2}\left(\frac{e}{R_x}\right)^2\left(\frac{x}{R_x}\right)^{\alpha_1}+O\left(\frac{\alpha_1}{2}\left(\frac{e}{R_x}\right)^2\left(\frac{x}{R_x}\right)^{\alpha_1}\right)\right) \tag{52}$$

In conclusion, since x remains of the order of R_x, the error is given by $\alpha_1(e/R_x)^2$. The error grows with e^2, which is consistent with the fact that the further the ship track is from the centre, the more we lose accuracy. The error is linear in α_1, so the steeper the profile, the larger the error. And the error decreases as R_x increases: large eddies are less affected by a shift e than small ones. For example, a Gaussian eddy of radius $100km$ sampled by a ship track shifted by $10km$ will have an error of 0.01, say 1%, which is quite small.

5.3 Velocity field and interpretation

We would like to say a few words about the velocity field resulting from the potential density field. Previous work has shown that the flow of mesoscale eddies is mainly driven by the cyclo-geostrophic balance (see the introduction). However, the Rossby number of eddies remains small (Cushman-Roisin et al., 1990). Let us therefore consider a mesoscale eddy under geostrophic balance. Its velocity can be retrieved on the $f-$ plane thanks to the thermal wind balance:

$$f_0\frac{\partial v_\theta}{\partial z} = -\frac{g}{\rho_0}\frac{\partial \sigma_0}{\partial r} \tag{53}$$

where f_0 is the Coriolis parameter, g, the gravity and ρ_0 the density of pure water. Reinjecting equation (42) in this expression and integrating with the boundary condition $v_\theta(r, z = -H_\infty) = 0$ (we consider that there is a geopotential level where the flow completely vanishes) leads to:

$$v_\theta(r,z) = -\frac{\alpha\psi_0}{f_0 R}\left(\frac{r}{R_1}\right)^{\alpha_1-1}\exp\left(-\left(\frac{r}{R_1}\right)^{\alpha_1}\right)\int_{-H_\infty}^{z}\frac{d\overline{\sigma_0}}{dz'}\left(\frac{z'-z_1}{H_1}\right)\exp\left(-\left(\frac{z'-z_1}{H_1}\right)^2\right)dz' \tag{54}$$

which is the total azimuthal velocity field. In the case the stratification is constant $d\overline{\sigma_0}/dz = cste$, we have:

$$v_\theta(r,z) = \frac{\alpha\psi_0}{2f_0R}\left(\frac{r}{R_1}\right)^{\alpha_1-1}\exp\left(-\left(\frac{r}{R_1}\right)^{\alpha_1}-\left(\frac{z'-z_1}{H_1}\right)^2\right) \tag{55}$$

For Gaussian vortices, this is exactly the formula proposed by (Bonnier et al., 2000; Negretti & Billant, 2013; Mahdinia et al., 2017) when they studied vortices in media with constant stratification. With this part we prove that the local stratification affects the velocity field and that vertically Gaussian eddies are an exception.

5.4 Sea surface elevation

As said in the introduction, a lot of studies based their analysis on satellites data. We can thus wonder if any information on the vertical profiles of eddies can be found through the sea surface elevation. In this last part, we chose to investigate this question using the quasi-geostrophic approximation as it provides powerful tools to relate the surface and subsurface signature of mesoscale eddies.

Considering rotating stratified flows, we work in the framework of the continuously stratified quasi-geostrophic (QG) equations. We assume that the ocean is infinitely deep. The equations require two conditions to be satisfied by the flow: a small Rossby number ($Ro = V/f_0R$) and an order one Burger number ($Bu = (N_0H_1/f_0R_1)^2 \sim 1$), where N_0 and f_0 are the stratification and rotation pulsations, H_1 and R_1 are the vertical and horizontal scales of the vortex. In this context, the QG stream function Ψ do the link between the buoyancy anomaly $\delta b = -g\frac{\delta\sigma_0}{\rho_0}$, where ρ_0 is chosen as the density of pure water, and the sea surface elevation η_s by the following equations:

$$\delta b = f_0\frac{\partial\Psi}{\partial z} \tag{56}$$

$$\eta_s = \frac{f_0}{g}\Psi(r, z=0) \tag{57}$$

Using the previously introduced notations, one can write:

$$\delta b(r,z) = \psi_0\overline{N}^2\left(\frac{z-z_1}{H_1}\right)\exp\left(-\left(\frac{z-z_1}{H_1}\right)^2-\left(\frac{r}{R_1}\right)^{\alpha_1}\right) \tag{58}$$

where $\overline{N}^2$ is the stratification pulsation of the ocean at rest and $\psi_0[m]$ the amplitude of the anomaly. Integrating the expression and expressing the result at $z = 0$ leads to:

$$\eta_s(r) = \frac{\psi_0}{g}\exp\left(-\left(\frac{r}{R_1}\right)^{\alpha_1}\right)\int_{-H_\infty}^{0}\overline{N}^2(z')\left(\frac{z'-z_1}{H_1}\right)\exp\left(-\left(\frac{z'-z_1}{H_1}\right)^2\right)dz' \tag{59}$$

Then, we introduce the adimentionalized quantities $\overline{r} = r/R_1$, $\overline{z} = (z-z_1)/H_1$, $\hat{N}^2 = \overline{N}^2/N_0^2$. The sea surface elevation is thus given by:

$$\eta_s(\overline{r}) = \frac{\psi_0H_1N_0^2}{g}e^{-\overline{r}^{\alpha_1}}\int_{\frac{-H_\infty-z_1}{H_1}}^{\frac{-z_1}{H_1}}\overline{z}e^{-\overline{z}^2}\hat{N}^2(H_1\overline{z}+z_1)d\overline{z} \tag{60}$$

The QG approximation is valid in the case $|\eta_s| \ll H_1$ or when $\psi_0 I \ll \frac{g}{N_0^2} \approx 10^4 m$ where I is the integral in the latter expression. Without approximation on $\hat{N}^2$, finding a value for I is difficult and we leave it for further studies. However, the expression proves that, in the absence of atmospheric forcing, the sea surface elevation does provide information on the vertical structure of mesoscale eddies. The sea surface elevation is driven by the local stratification.

6 Conclusion

In this work, we have studied the 3D structure of anticyclonic eddies sampled by *in situ* observations carried out during oceanographic cruises. In contrast to previous contributions on this topic, which mainly focused on the velocity field, we were interested in analysing the potential density field, which acts as a backbone to sustain the flow in the core of the eddy and provides the key process for maintaining the coherence of the eddy. We have shown that the presence of the eddy in a stratified medium induces two density anomalies. One is due to the slope of the isopycnals, and the other is due to the fact that oceanic mesoscale eddies advect remaining water masses into their core, creating thermohaline anomalies on the isopycnals. However, this second term appears to be much smaller than the first.

We have also analysed the shapes of these density anomalies. Horizontally, the alpha-exponential formula proposed by previous studies was found to be suitable for modelling density anomalies. However, the value of the isopycnal slope steepness can exceed 3, which was not predicted by previous studies on this topic. Then, vertically, we showed that Gaussian anomalies are an exception and that the anomaly is also driven by local stratification. As a result, eddies do not appear to be symmetric with respect to their median plane.

The relationship between what is observed on 2D vertical sections and the real 3D structure of eddies was also an important issue we tried to address. We saw that if the eddy was sampled by a ship track passing close enough to the centre, the 2D vertical sections were representative of the actual 3D eddy structure. We also showed that the error depends on the steepness of the profile as well as the radius of the eddy.

However, this study has several limitations. One is that we only studied anticyclonic eddies. The same work needs to be carried out on their cyclonic counterparts. Also, in situ experiments tend to sample the upper layers of the ocean much more intensively than the deeper layers. As a result, the base of mesoscale eddies on 2D vertical sections suffers from some distortion during interpolation. The instruments often do not reach the point where the anomalies disappear completely. In the future, the proposed formulation for the total potential density field needs to be validated with more cases.

Acknowledgments

This research has been supported by the European Union Horizon2020 research and innovation program under grant agreements no. 817578 (TRIATLAS), the Centre National d'Etudes Spatiales through the TOEddies and EUREC4A-OA projects, the French national programme LEFE INSU, IFREMER, the French vessel research fleet, the French research infrastructures AERIS and ODATIS, IPSL, the Chaire Chanel programme of the Geosciences Department at ENS, and the EUREC4A-OA JPI Ocean and Climate programme. We would also like to thank the captains, crews and scientists of the RVs Atalante, Maria S. Merian, Meteor and Kristine Bonnevie. Yan Barabinot is supported by a Ph.D grant from Ecole Normale Supérieure de Saclay. Xavier Carton acknowledges support by UBO and by a CNES contract EUREC4A-OA.

We benefited from numerous data sets freely available and listed here. The concatenated RVs Atalante and Maria S Merian hydrographic data are freely available on the SEANOE website: https://www.seanoe.org/data/00809/92071/, accessed on 15 March 2021.

The hydrographic and velocity measurements taken during the M124 cruise of the RV Meteor are freely available on the PANGAEA web site: https://doi.org/10.1594/PANGAEA.902947, https://doi.org/10.1594/PANGAEA.895426, https://doi.org/10.1594/PANGAEA.863017, https://doi.org/10.1594/PANGAEA.863015, https://doi.org/10.1594/PANGAEA.869740.

Finally, hydrographic and velocity measurements along Physindien 2011 are freely available on Ifremer website: https://co-en.ifremer.fr/eulerianPlatform?startDate=29%2F01%2F2014&endDate=28%2

References

Aguedjou, H. M. A., Chaigneau, A., Dadou, I., Morel, Y., Pegliasco, C., Da-Allada, C. Y., & Baloïtcha, E. (2021). What can we learn from observed temperature and salinity isopycnal anomalies at eddy generation sites? application in the tropical atlantic ocean. *Journal of Geophysical Research: Oceans*, *126*(11), e2021JC017630.

Aubert, O., Bars, M. L., Gal, P. L., & Marcus, P. S. (2012). The universal aspect ratio of vortices in rotating stratified flows: experiments and observations. *Journal of Fluid Mechanics*, *706*, 34 - 45. Retrieved from `https://api.semanticscholar.org/CorpusID:13873931`

Ayouche, A., De Marez, C., Morvan, M., L'hegaret, P., Carton, X., Le Vu, B., & Stegner, A. (2021). Structure and dynamics of the ras al hadd oceanic dipole in the arabian sea. In *Oceans* (Vol. 2, pp. 105–125).

Barabinot, Y., Speich, S., & Carton, X. J. (2023). Defining mesoscale eddies boundaries from in-situ data and a theoretical framework. *Authorea*. doi: 10.22541/essoar.167870447.76933252/v1

Bennani, Y., Ayouche, A., & Carton, X. (2022). 3d structure of the ras al hadd oceanic dipole. In *Oceans* (Vol. 3, pp. 268–288).

Beron-Vera, F. J., Wang, Y., Olascoaga, M. J., Goñi, G., & Haller, G. (2013). Objective detection of oceanic eddies and the agulhas leakage. *Journal of Physical Oceanography*, *43*, 1426-1438.

Bonnier, M., Eiff, O., & Bonneton, P. (2000). On the density structure of far-wake vortices in a stratified fluid. *Dynamics of Atmospheres and oceans*, *31*(1-4), 117–137.

Bretherton, F. P. (1966). Critical layer instability in baroclinic flows. *Quarterly Journal of the Royal Meteorological Society*, *92*(393), 325–334.

Bryden, H. L. (1979). Poleward heat flux and conversion of available potential energy in drake passage. *Journal of Marine Research*, *37*, 1-12.

Cao, Y., Dong, C., Stegner, A., Bethel, B. J., Li, C., Dong, J., ... Yang, J. (2023). Global sea surface cyclogeostrophic currents derived from satellite altimetry data. *Journal of Geophysical Research: Oceans*, *128*(1), e2022JC019357.

Carton, X. (2001). Hydrodynamical modeling of oceanic vortices. *Surveys in Geophysics*, *22*, 179-263. Retrieved from `https://api.semanticscholar.org/CorpusID:123836410`

Carton, X., Flierl, G. R., Perrot, X., Meunier, T., & Sokolovskiy, M. A. (2010). Explosive instability of geostrophic vortices. part 1: baroclinic instability. *Theoretical and Computational Fluid Dynamics*, *24*, 125-130.

Carton, X., & McWilliams, J. C. (1989). Barotropic and baroclinic instabilities of axisymmetric vortices in a quasigeostrophic model. *Elsevier oceanography series*, *50*, 225-244.

Chaigneau, A., Eldin, G., & Dewitte, B. (2009). Eddy activity in the four major upwelling systems from satellite altimetry (1992-2007). *Progress in Oceanography*, *83*, 117-123.

Chaigneau, A., Gizolme, A., & Grados, C. (2008). Mesoscale eddies off peru in altimeter records: Identification algorithms and eddy spatio-temporal patterns. *Progress in Oceanography*, *79*(2-4), 106–119.

Chaigneau, A., Le Texier, M., Eldin, G., Grados, C., & Pizarro, O. (2011). Vertical structure of mesoscale eddies in the eastern south pacific ocean: A composite analysis from altimetry and argo profiling floats. *Journal of Geophysical Research: Oceans*, *116*(C11).

Chelton, D., Schlax, M. G., & Samelson, R. M. (2011). Global observations of nonlinear mesoscale eddies. *Progress in Oceanography*, *91*, 167-216.

Chelton, D. B., Schlax, M. G., Samelson, R. M., & de Szoeke, R. A. (2007). Global observations of large oceanic eddies. *Geophysical Research Letters*, *34*(15).

Chen, G., Han, G., & Yang, X. (2019). On the intrinsic shape of oceanic eddies derived from satellite altimetry. *Remote Sensing of Environment*, *228*, 75–89.

Cui, W., Zhou, C., Zhang, J., & Yang, J. (2021). Statistical characteristics and thermohaline properties of mesoscale eddies in the bay of bengal. *Acta Oceanologica Sinica*, *40*(4), 10–22.

Cushman-Roisin, B., Tang, B., & Chassignet, E. P. (1990). Westward motion of mesoscale eddies. *Journal of Physical Oceanography*, *20*(5), 758–768.

Douglass, E., & Richman, J. (2015). Analysis of ageostrophy in strong surface eddies in the a tlantic o cean. *Journal of Geophysical Research: Oceans*, *120*(3), 1490–1507.

Flierl, G. R. (1981). Particle motions in large-amplitude wave fields. *Geophysical and Astrophysical Fluid Dynamics*, *18*, 39-74.

Flór, J.-B. (1994). *Coherent vortex structures in stratified fluids* (Phd Thesis 1 (Research TU/e / Graduation TU/e), Applied Physics and Science Education). (Proefschrift.) doi: 10.6100/IR417065

Frenger, I., Gruber, N., Knutti, R., & Münnich, M. (2013). Imprint of southern ocean eddies on winds, clouds and rainfall. *Nature Geoscience*, *6*, 608-612.

Haller, G. (2015). Lagrangian coherent structures. *Annual Review of Fluid Mechanics*, *47*, 137-162. Retrieved from `https://api.semanticscholar.org/CorpusID:122894798`

Jayne, S. R., & Marotzke, J. (2002). The oceanic eddy heat transport. *Journal of Physical Oceanography*, *32*, 3328-3345.

Karstensen, J., Sabrina, S., Raphael, M., Karl, B., Jennifer, C., Marco, G., ... Andreas, R. (2016). *Oceanic & atmospheric variability in the south atlantic, cruise no. m124* (Vol. M124). Retrieved from `https://doi.org/10.1594/PANGAEA.869740`

Kolmogorov, A. N. (1941). Equations of turbulent motion in an incompressible fluid. *Proceedings of the USSR Academy of Sciences*, *30*, 299-303. Retrieved from `https://api.semanticscholar.org/CorpusID:118472206`

Laxenaire, R., Speich, S., Blanke, B., Chaigneau, A., Pegliasco, C., & Stegner, A. (2018). Anticyclonic eddies connecting the western boundaries of indian and atlantic oceans. *Journal of Geophysical Research: Oceans*.

Laxenaire, R., Speich, S., & Stegner, A. (2019). Evolution of the thermohaline structure of one agulhas ring reconstructed from satellite altimetry and argo floats. *Journal of Geophysical Research*, *124*, 8969-9003.

Laxenaire, R., Speich, S., & Stegner, A. (2020). Agulhas ring heat content and transport in the south atlantic estimated by combining satellite altimetry and argo profiling floats data. *Journal of Geophysical Research*, *125*.

Legras, B., & Dritschel, D. G. (1993). Vortex stripping and the generation of high vorticity gradients in two-dimensional flows. *Flow Turbulence and Combustion*, *51*, 445–455.

L'Hégaret, P., Schütte, F., Speich, S., Reverdin, G., Baranowski, D. B., Czeschel, R., ... others (2022). Ocean cross-validated observations from the r/vs l'atalante, maria s. merian and meteor and related platforms as part of the eurec 4 a-oa/atomic campaign. *Earth System Science Data Discussions*, 1–39.

Lin, X., Qiu, Y., & Sun, D. (2019). Thermohaline structures and heat/freshwater transports of mesoscale eddies in the bay of bengal observed by argo and satellite data. *Remote Sensing*, *11*(24), 2989.

Lozier, M. S. (1997). Evidence for large-scale eddy-driven gyres in the north atlantic. *Science*, *277*, 361-364.

Mahdinia, M., Hassanzadeh, P., Marcus, P. S., & Jiang, C.-H. (2017). Stability

of three-dimensional gaussian vortices in an unbounded, rotating, vertically stratified, boussinesq flow: Linear analysis. *Journal of Fluid Mechanics*, *824*, 97–134.

Mariotti, A., Legras, B., & Dritschel, D. G. (1994). Vortex stripping and the erosion of coherent structures in two-dimensional flows. *Physics of Fluids*, *6*, 3954–3962.

McDougall, T. J., Jackett, D. R., Wright, D. G., & Feistel, R. (2003). Accurate and computationally efficient algorithms for potential temperature and density of seawater. *Journal of Atmospheric and Oceanic Technology*, *20*(5), 730–741.

McWilliams, J. C. (1984). The emergence of isolated coherent vortices in turbulent flow. *Journal of Fluid Mechanics*, *146*, 21 - 43. Retrieved from `https://api.semanticscholar.org/CorpusID:7002682`

McWilliams, J. C. (1985). Submesoscale, coherent vortices in the ocean. *Reviews of Geophysics*, *23*, 165-182. Retrieved from `https://api.semanticscholar.org/CorpusID:124265810`

McWilliams, J. C. (1989). Statistical properties of decaying geostrophic turbulence. *Journal of Fluid Mechanics*, *198*, 199 - 230. Retrieved from `https://api.semanticscholar.org/CorpusID:122801284`

McWilliams, J. C. (1990). The vortices of geostrophic turbulence. *Journal of Fluid Mechanics*, *219*, 387 - 404. Retrieved from `https://api.semanticscholar.org/CorpusID:123045316`

Morrow, R., Coleman, R., Church, J. A., & Chelton, D. (1994). Surface eddy momentum flux and velocity variances in the southern ocean from geosat altimetry. *Journal of Physical Oceanography*, *24*, 2050-2071.

Morrow, R., & Traon, P.-Y. L. (2012). Recent advances in observing mesoscale ocean dynamics with satellite altimetry. *Advances in Space Research*, *50*, 1062-1076.

Negretti, M. E., & Billant, P. (2013). Stability of a gaussian pancake vortex in a stratified fluid. *Journal of Fluid Mechanics*, *718*, 457–480.

Nencioli, F., Dall'Olmo, G., & Quartly, G. D. (2018). Agulhas ring transport efficiency from combined satellite altimetry and argo profiles. *Journal of Geophysical Research: Oceans*, *123*(8), 5874–5888.

Nencioli, F., Kuwahara, V. S., Dickey, T. D., Rii, Y. M., & Bidigare, R. R. (2008). Physical dynamics and biological implications of a mesoscale eddy in the lee of hawai'i : Cyclone opal observations during e-flux iii. *Deep-sea Research Part II-Topical Studies in Oceanography*, *55*, 1252–1274.

Oseen, C. (1912). Uber die wirbelbewegung in einer reibenden flussigkeit. *Ark. Mat. Astro. Fys.*, *7*.

Pegliasco, C., Chaigneau, A., & Morrow, R. (2015). Main eddy vertical structures observed in the four major eastern boundary upwelling systems. *Journal of Geophysical Research: Oceans*, *120*(9), 6008–6033.

Penven, P., Halo, I., Pous, S., & Marié, L. (2014). Cyclogeostrophic balance in the mozambique channel. *Journal of Geophysical Research*, *119*, 1054-1067. Retrieved from `https://api.semanticscholar.org/CorpusID:55086854`

Roquet, F., Madec, G., McDougall, T. J., & Barker, P. M. (2015). Accurate polynomial expressions for the density and specific volume of seawater using the teos-10 standard. *Ocean Modelling*, *90*, 29–43.

Sallée, J., Speer, K., Rintoul, S. R., & Wijffels, S. E. (2010). Southern ocean thermocline ventilation. *Journal of Physical Oceanography*, *40*, 509-529.

Smith, W. H. F., & Sandwell, D. T. (1997). Global sea floor topography from satellite altimetry and ship depth soundings. *Science*, *277*, 1956-1962.

Souza, J., de Boyer Montégut, C., Cabanes, C., & Klein, P. (2011). Estimation of the agulhas ring impacts on meridional heat fluxes and transport using argo floats and satellite data. *Geophysical Research Letters*, *38*(21).

Speich, S., & Team, E. S. (2021). *Eurec4a-oa cruise report, 19 january - 19 february*

2020, vessel : L'atalante. Retrieved from http://doi.org/10.13155/80129 doi: 10.13155/80129

Stevens, B., Bony, S., Farrell, D., Ament, F., Blyth, A., Fairall, C., ... Zöger, M. (2021). Eurec^{4}a. *Earth System Science Data*, *13*(8), 4067–4119. Retrieved from https://essd.copernicus.org/articles/13/4067/2021/ doi: 10.5194/essd-13-4067-2021

Subirade, C., L'Hégaret, P., Speich, S., Laxenaire, R., Karstensen, J., & Carton, X. (2023). Combining an eddy detection algorithm with in-situ measurements to study north brazil current rings. *Remote. Sens.*, *15*, 1897.

Tychensky, A., & Carton, X. (1998). Hydrological and dynamical characterization of meddies in the azores region: a paradigm for baroclinic vortex dynamics. *Journal of Geophysical Research: Oceans*, *103*(C11), 25061–25079.

Wunsch, C. (1999). Where do ocean eddy heat fluxes matter. *Journal of Geophysical Research*, *104*, 13235-13249.

Yang, B., Fox, J., Behrenfeld, M. J., Boss, E. S., Haëntjens, N., Halsey, K. H., ... Doney, S. C. (2021). In situ estimates of net primary production in the western north atlantic with argo profiling floats. *Journal of Geophysical Research: Biogeosciences*, *126*(2), e2020JG006116.

Yang, Y., Zeng, L., & Wang, Q. (2021). How much heat and salt are transported into the south china sea by mesoscale eddies? *Earth's Future*, *9*(7), e2020EF001857.

Figure 1.

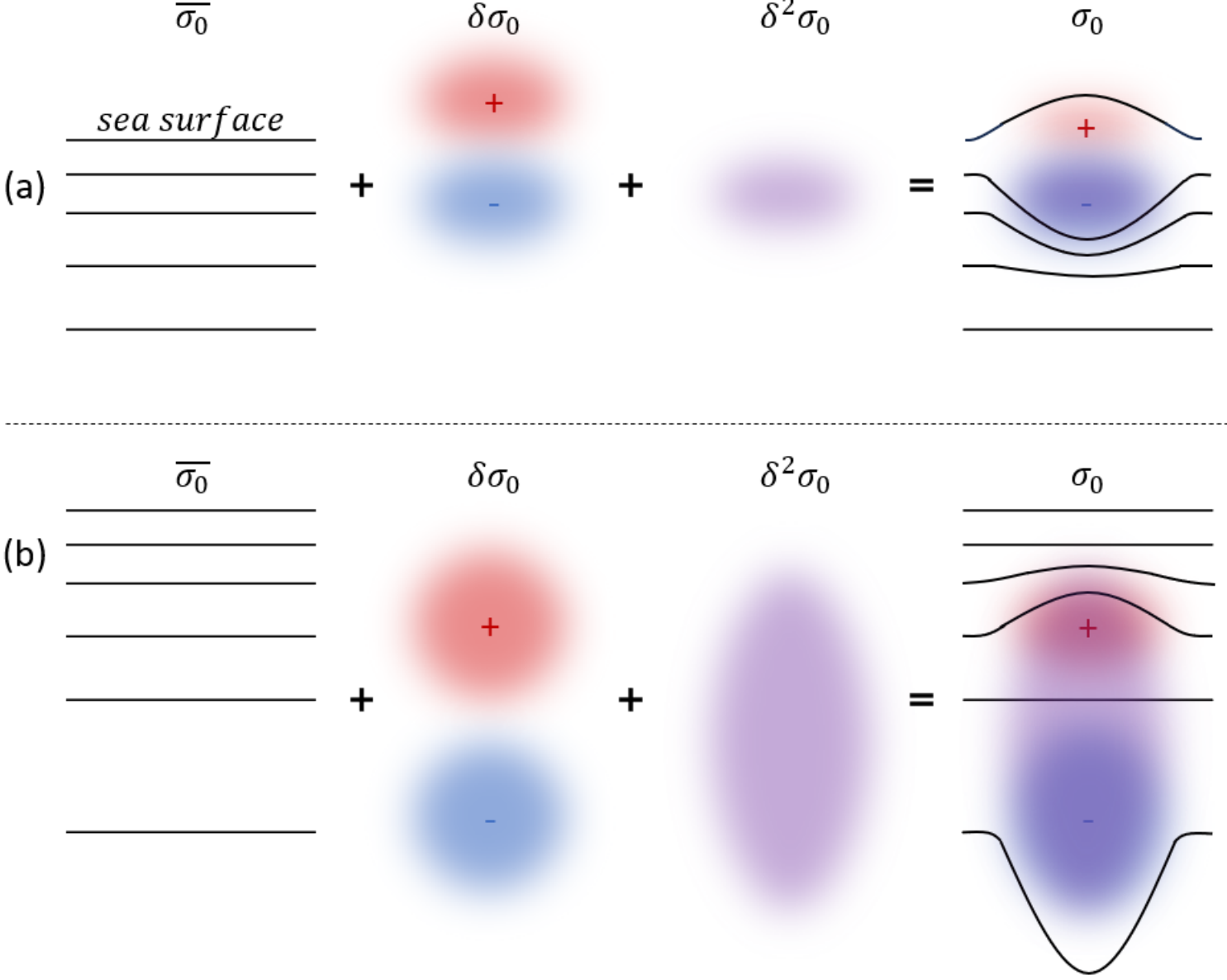
$\overline{\sigma_0}$
$\delta\sigma_0$
$\delta^2\sigma_0$
σ_0
sea surface
(a)
+
+
=
+
-
$\overline{\sigma_0}$
$\delta\sigma_0$
$\delta^2\sigma_0$
σ_0
(b)
+
+
=
+
-

Figure 2.

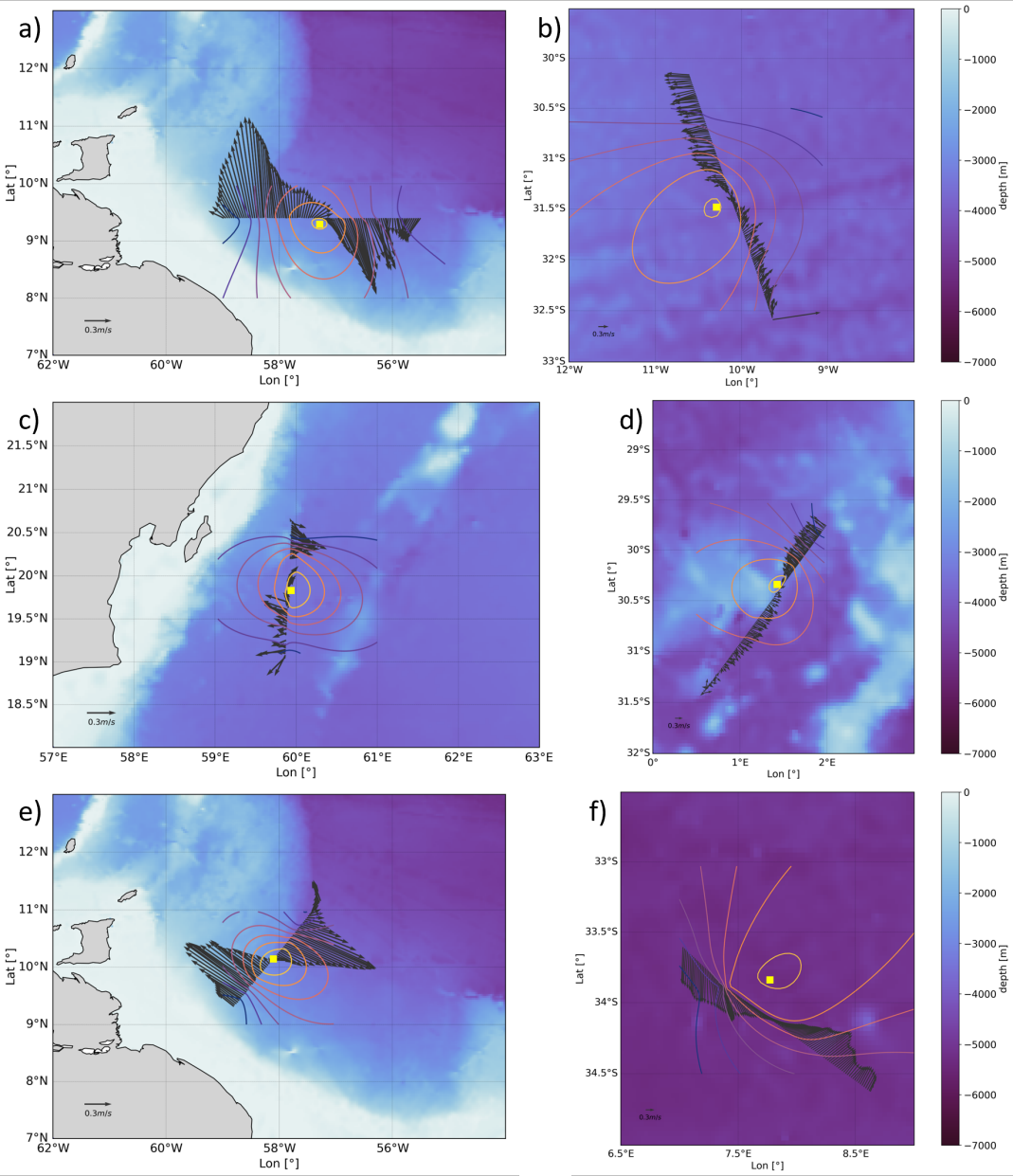
a)
12°N
11°N
10°N
9°N
8°N
7°N
Lat [°]
62°W
60°W
58°W
56°W
Lon [°]
0.3m/s
b)
30°S
30.5°S
31°S
31.5°S
32°S
32.5°S
33°S
Lat [°]
12°W
11°W
10°W
9°W
Lon [°]
0.3m/s
0
−1000
−2000
−3000
−4000
−5000
−6000
−7000
depth [m]
c)
21.5°N
21°N
20.5°N
20°N
19.5°N
19°N
18.5°N
Lat [°]
57°E
58°E
59°E
60°E
61°E
62°E
63°E
Lon [°]
0.3m/s
d)
29°S
29.5°S
30°S
30.5°S
31°S
31.5°S
32°S
Lat [°]
0°
1°E
2°E
Lon [°]
0.3m/s
e)
12°N
11°N
10°N
9°N
8°N
7°N
Lat [°]
62°W
60°W
58°W
56°W
Lon [°]
0.3m/s
f)
33°S
33.5°S
34°S
34.5°S
Lat [°]
6.5°E
7.5°E
8.5°E
Lon [°]
0.3m/s

Figure 3.

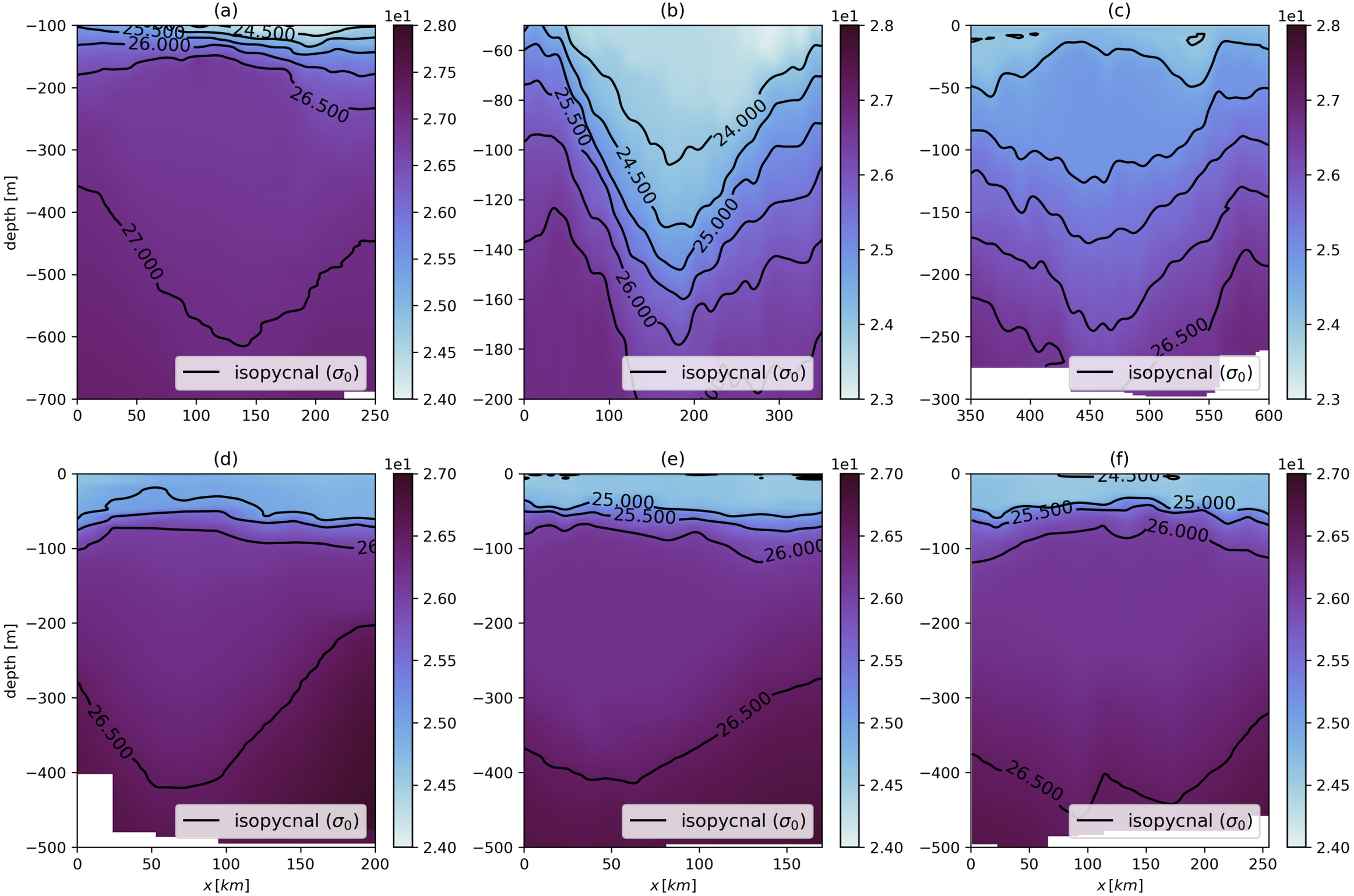
(a)
(b)
(c)
(d)
(e)
(f)
depth [m]
x [km]
1e1
isopycnal (σ_0)
25.500
26.000
26.500
27.000
24.500
24.000
25.000

Figure 4.

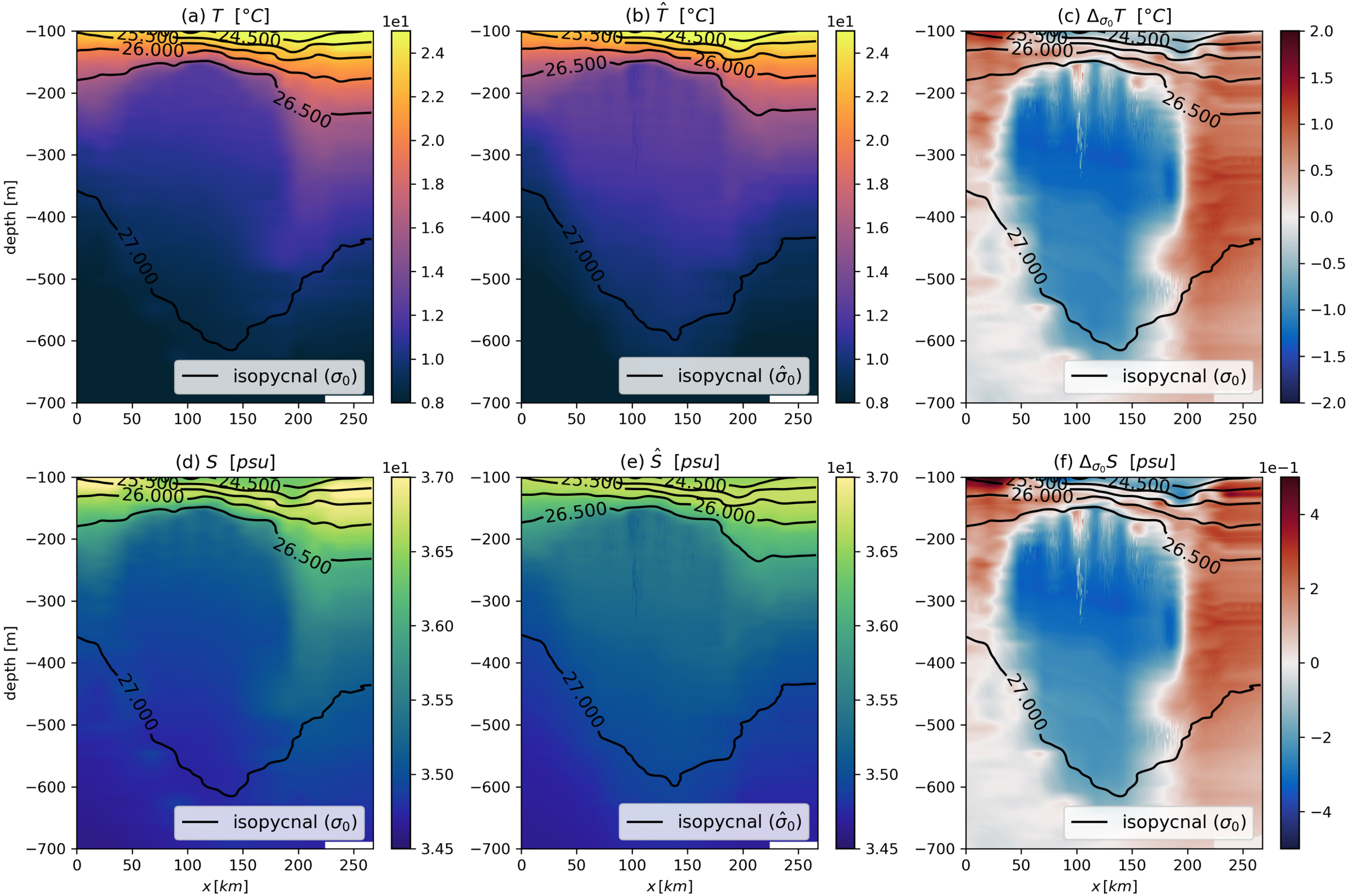
(a) T [°C]
(b) $\hat{T}$ [°C]
(c) $\Delta_{\sigma_0} T$ [°C]
(d) S [psu]
(e) $\hat{S}$ [psu]
(f) $\Delta_{\sigma_0} S$ [psu]
depth [m]
x [km]
isopycnal (σ_0)
isopycnal ($\hat{\sigma}_0$)
25.500
24.500
26.000
26.500
27.000
1e1
1e−1

Figure 5.

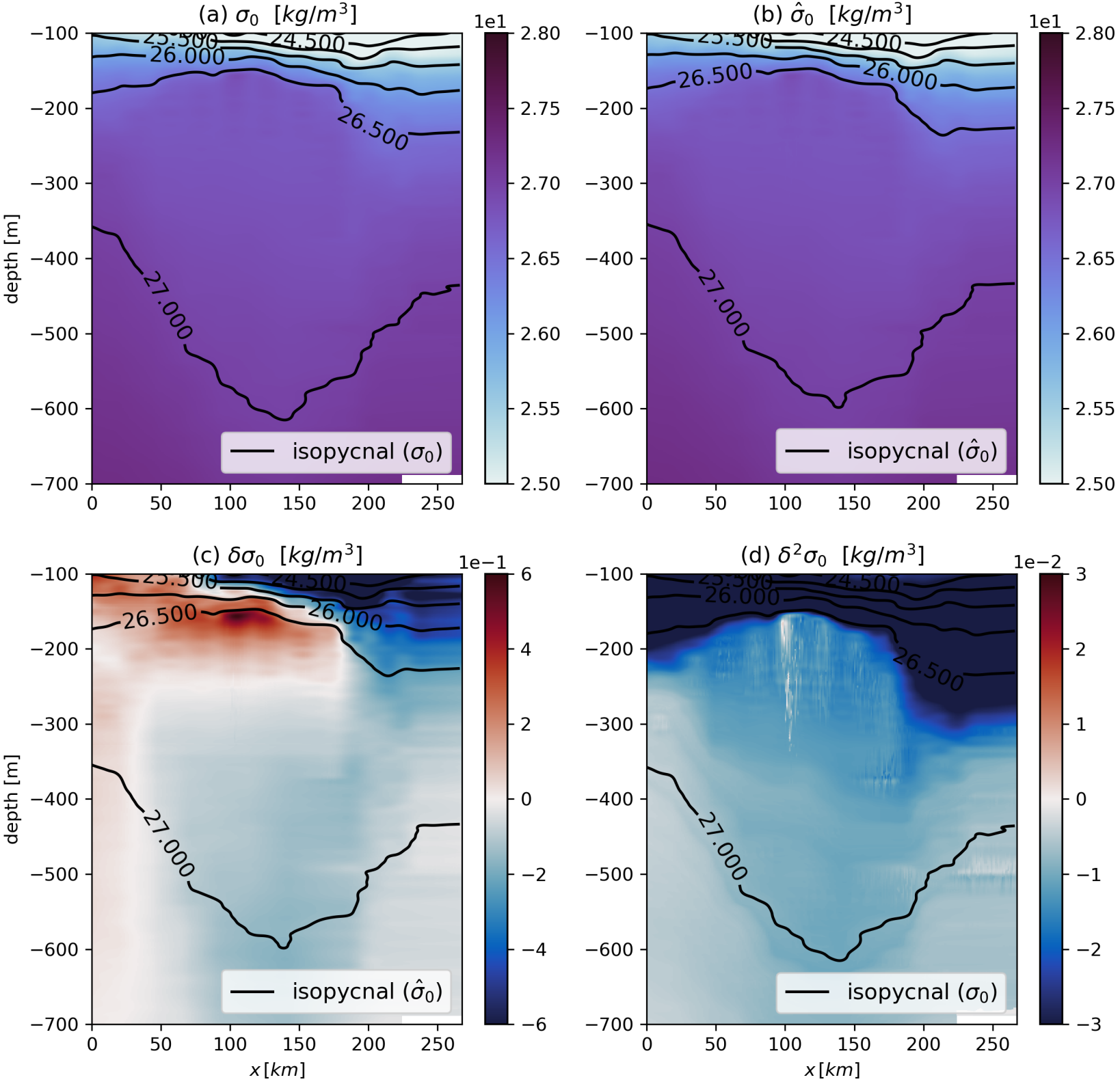
(a) σ_0 [kg/m^3]
(b) $\hat{\sigma}_0$ [kg/m^3]
(c) $\delta\sigma_0$ [kg/m^3]
(d) $\delta^2\sigma_0$ [kg/m^3]
25.500
24.500
26.000
26.500
27.000
isopycnal (σ_0)
isopycnal ($\hat{\sigma}_0$)
1e1
1e−1
1e−2
depth [m]
x [km]

Figure 6.

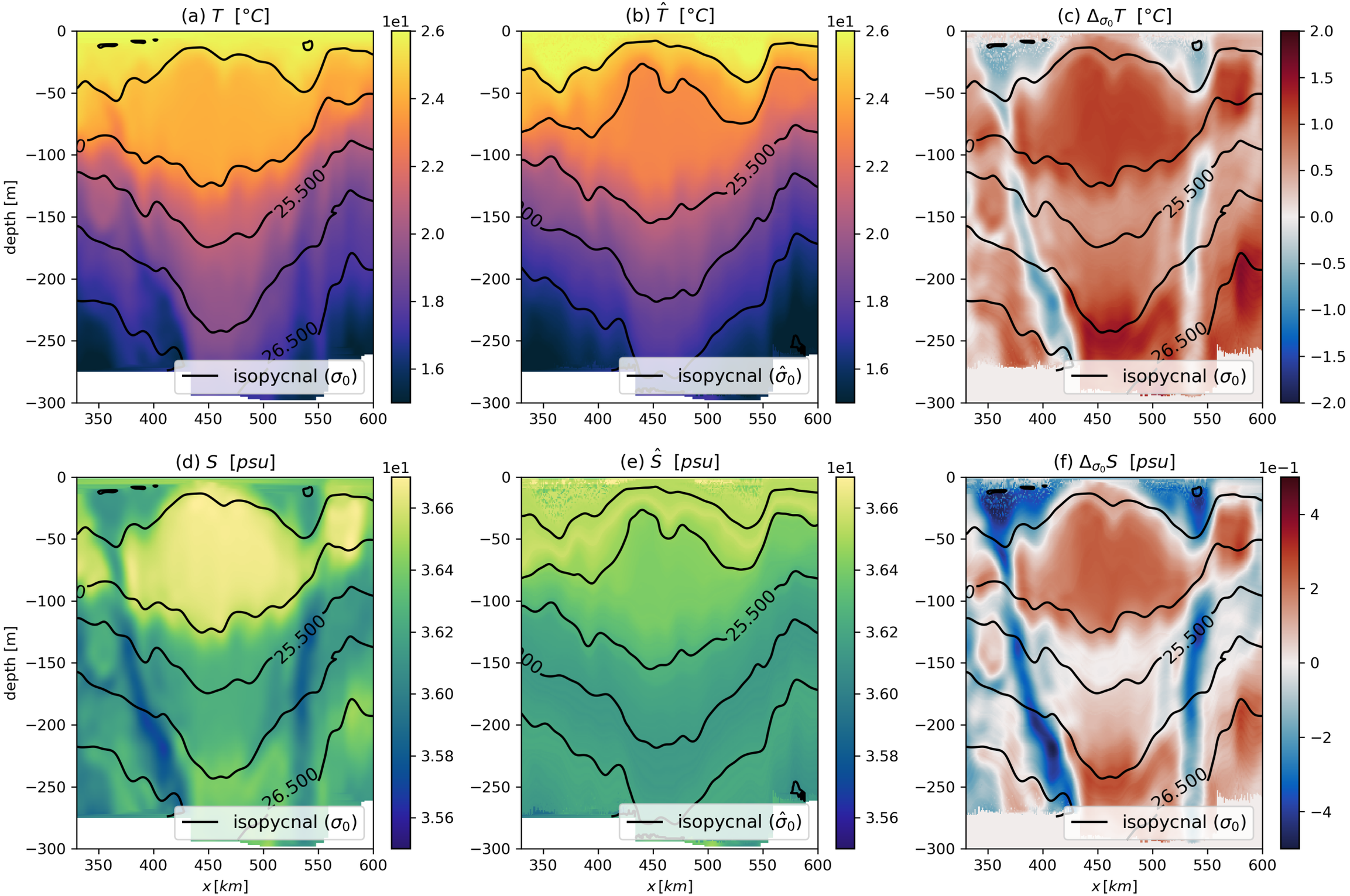
(a) T [°C]
(b) $\hat{T}$ [°C]
(c) $\Delta_{\sigma_0} T$ [°C]
(d) S [psu]
(e) $\hat{S}$ [psu]
(f) $\Delta_{\sigma_0} S$ [psu]
depth [m]
x [km]
1e1
1e−1
25.500
26.500
isopycnal (σ_0)
isopycnal ($\hat{\sigma}_0$)

Figure 7.

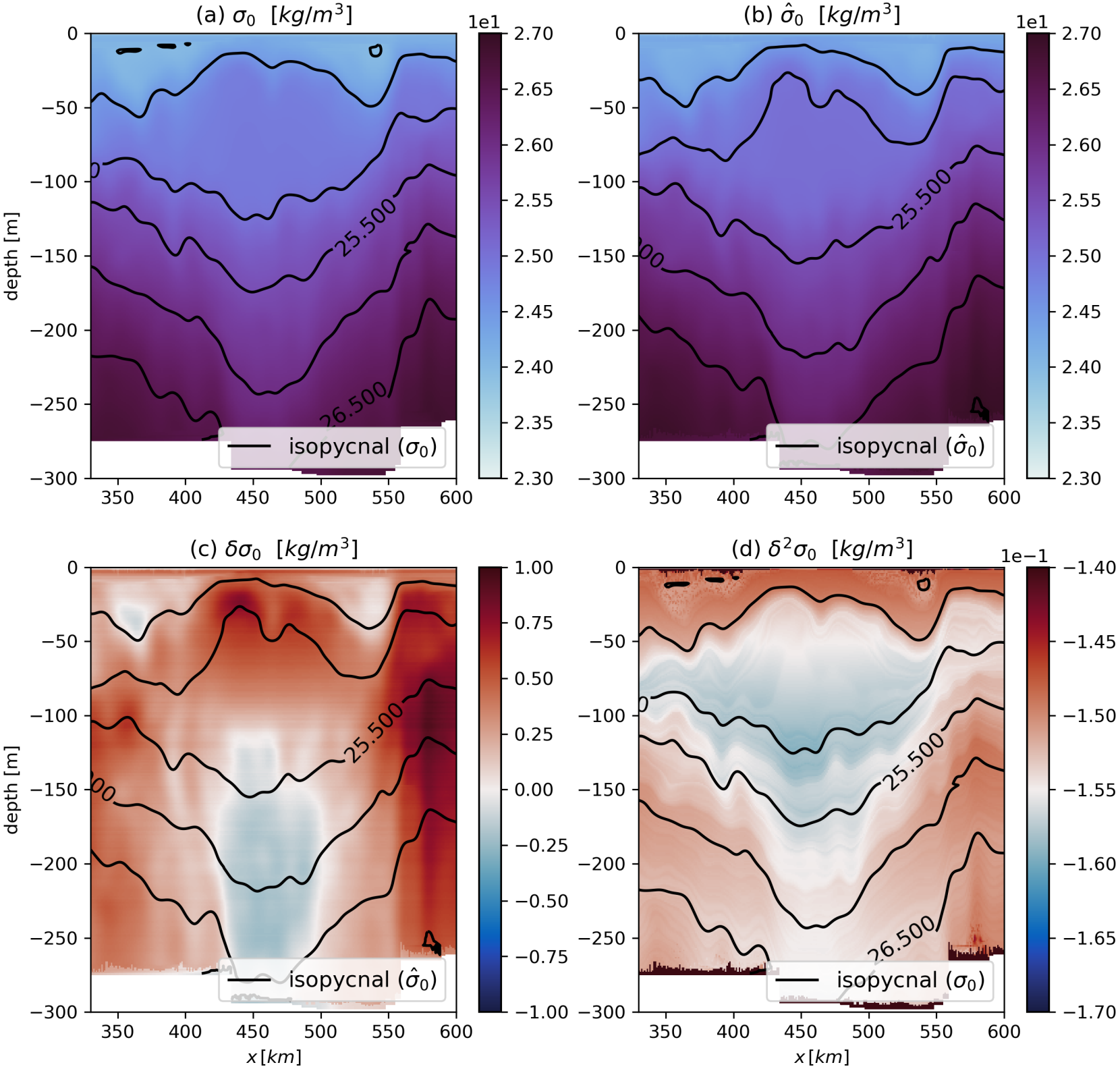
(a) σ_0 $[kg/m^3]$
(b) $\hat{\sigma}_0$ $[kg/m^3]$
(c) $\delta\sigma_0$ $[kg/m^3]$
(d) $\delta^2\sigma_0$ $[kg/m^3]$
depth [m]
x [km]
25.500
26.500
isopycnal (σ_0)
isopycnal ($\hat{\sigma}_0$)
1e1
1e−1

Figure 8.

(a) $RMS = 5.52\%$, $\psi_0 = 146m$, $z_1 = -54.6m$, $H_1 = 139.4m$, $B = 2.4m$

(b) $RMS = 8.0\%$, $\psi_0 = 276m$, $z_1 = -343m$, $H_1 = 385m$, $B = -71.8m$

(c) $RMS = 13.2\%$, $\psi_0 = 78m$, $z_1 = -73.5m$, $H_1 = 43.4m$, $B = -2.7m$

(d) $RMS = 5.3\%$, $\psi_0 = 56.5m$, $z_1 = -243m$, $H_1 = 157.4m$, $B = -6.2m$

(e) $RMS = 9.55\%$, $\psi_0 = 77.9m$, $z_1 = -226m$, $H_1 = 125.8m$, $B = -8.1m$

(f) $RMS = 9.82\%$, $\psi_0 = 41.5m$, $z_1 = -200m$, $H_1 = 99.2m$, $B = 3.8m$

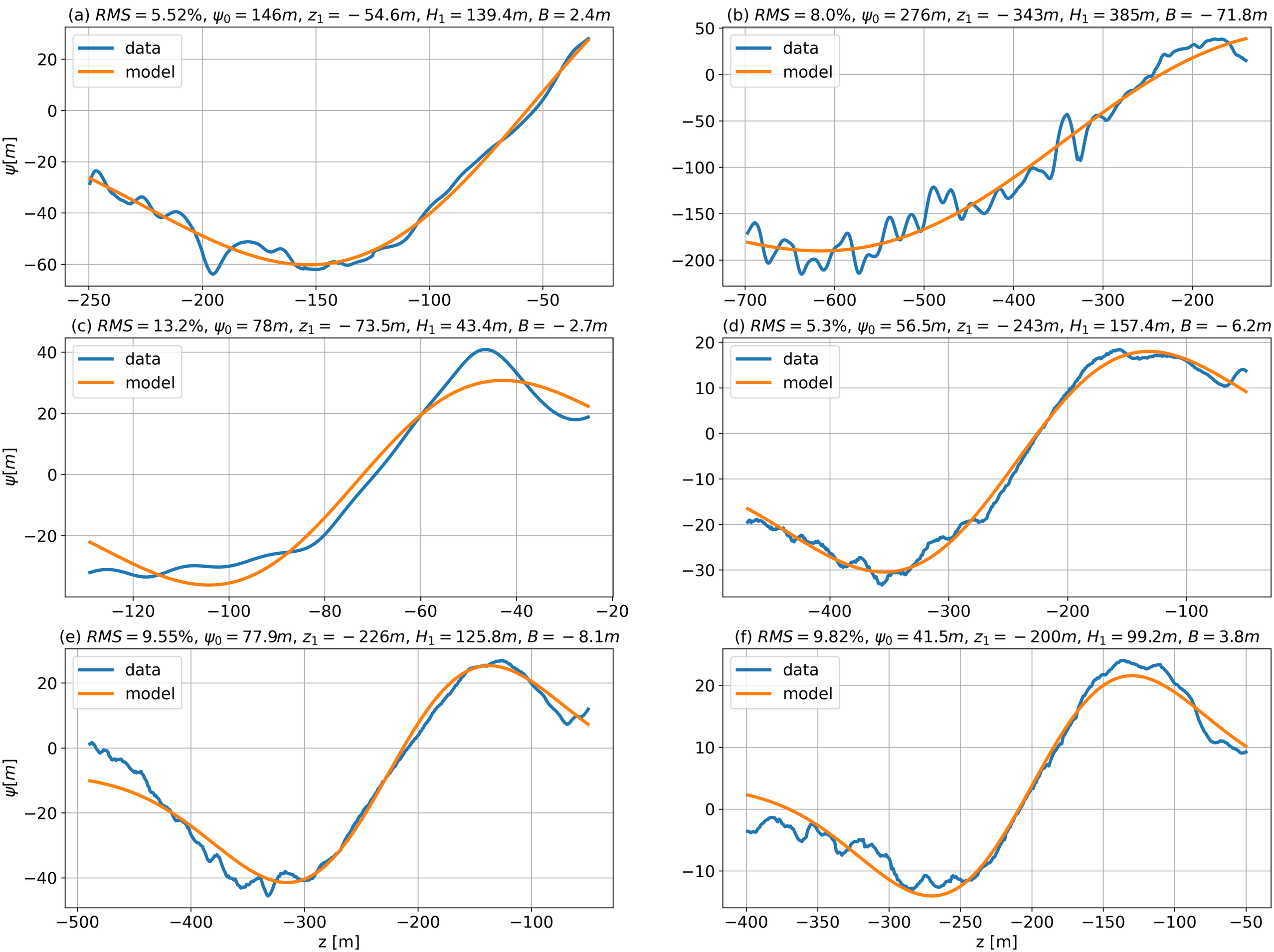

Figure 9.

(a) $RMS = 8.5\%$, $x_1 = 184km$, $R_1 = 47.1km$, $\alpha_1 = 2$

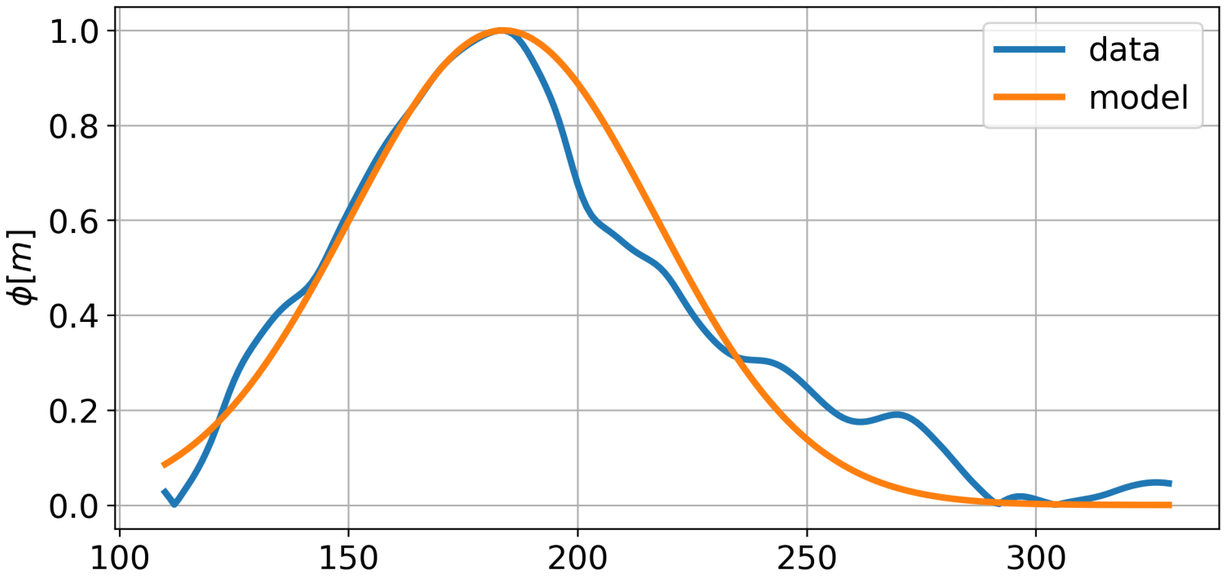

(b) $RMS = 6.8\%$, $x_1 = 99.6km$, $R_1 = 87.83km$, $\alpha_1 = 6$

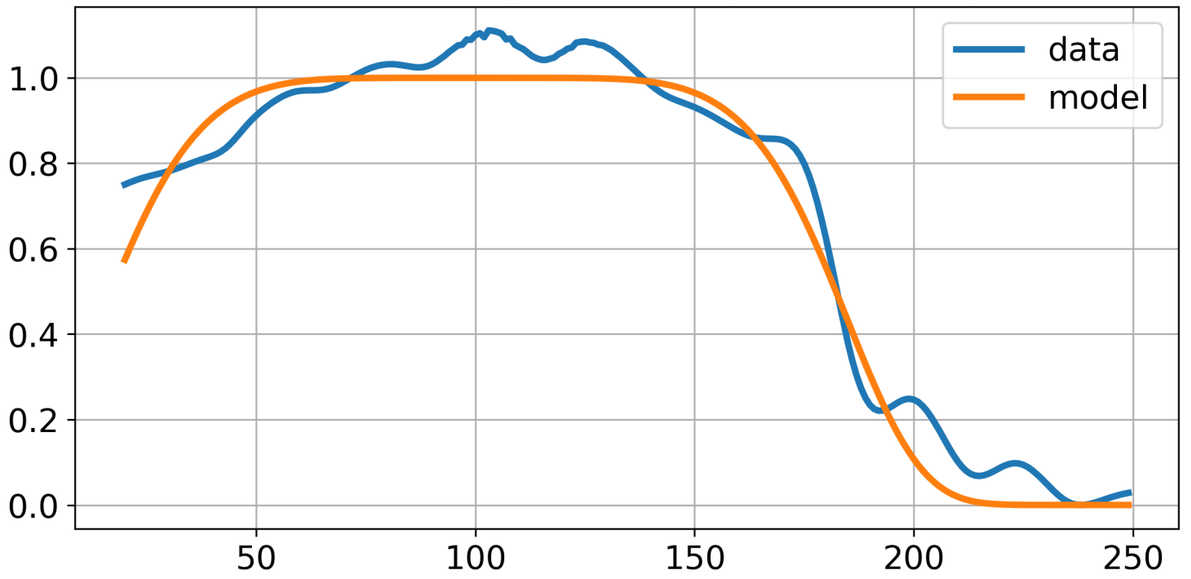

(c) $RMS = 5.24\%$, $x_1 = 462km$, $R_1 = 56km$, $\alpha_1 = 4$

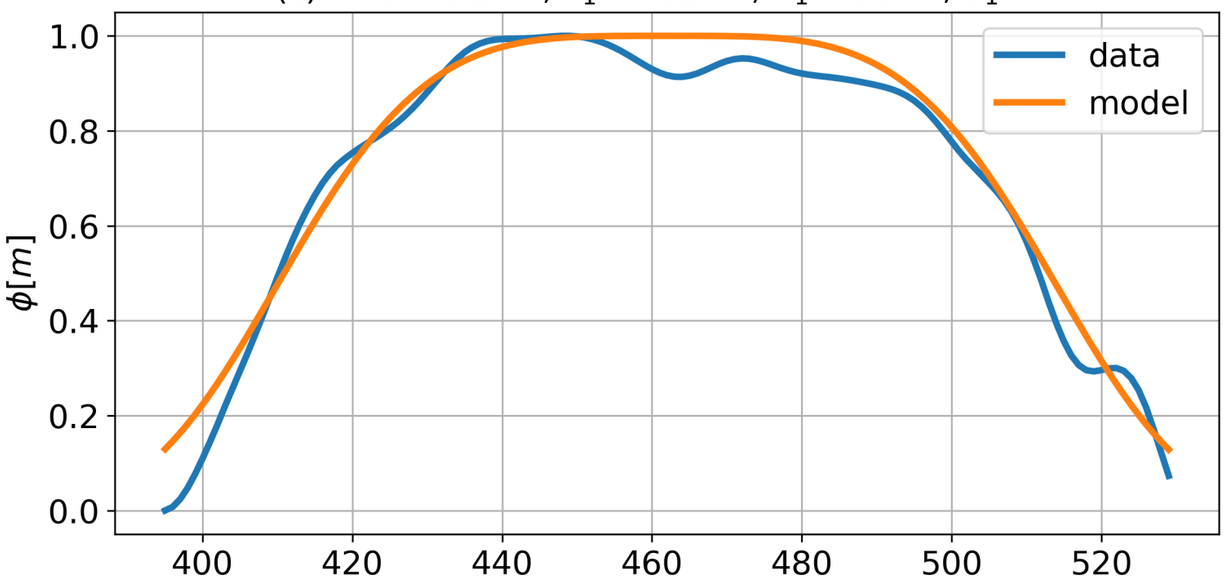

(d) $RMS = 6.3\%$, $x_1 = 72km$, $R_1 = 50km$, $\alpha_1 = 2$

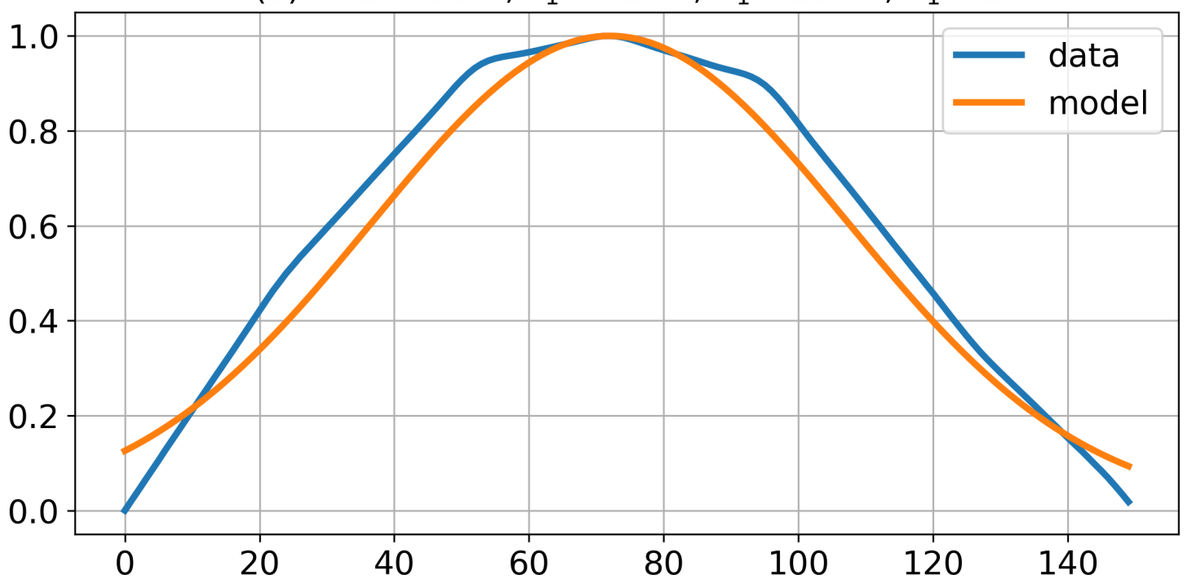

(e) $RMS = 4.7\%$, $x_1 = 48.3km$, $R_1 = 70km$, $\alpha_1 = 4$

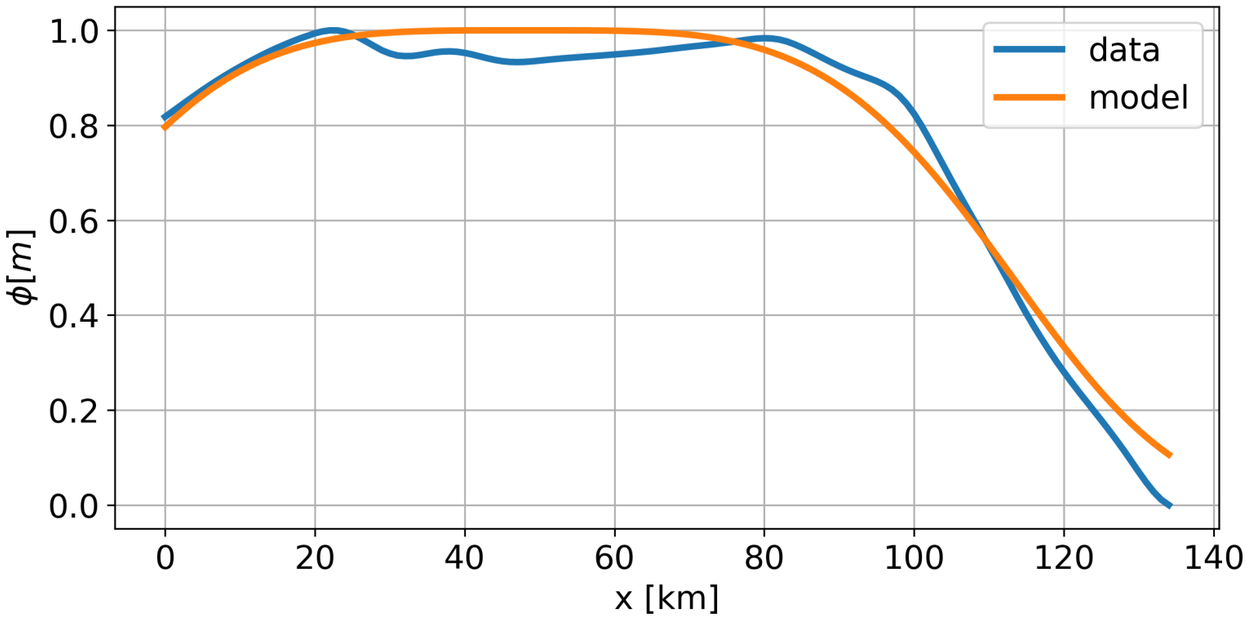

(f) $RMS = 7.1\%$, $x_1 = 131km$, $R_1 = 102km$, $\alpha_1 = 6$

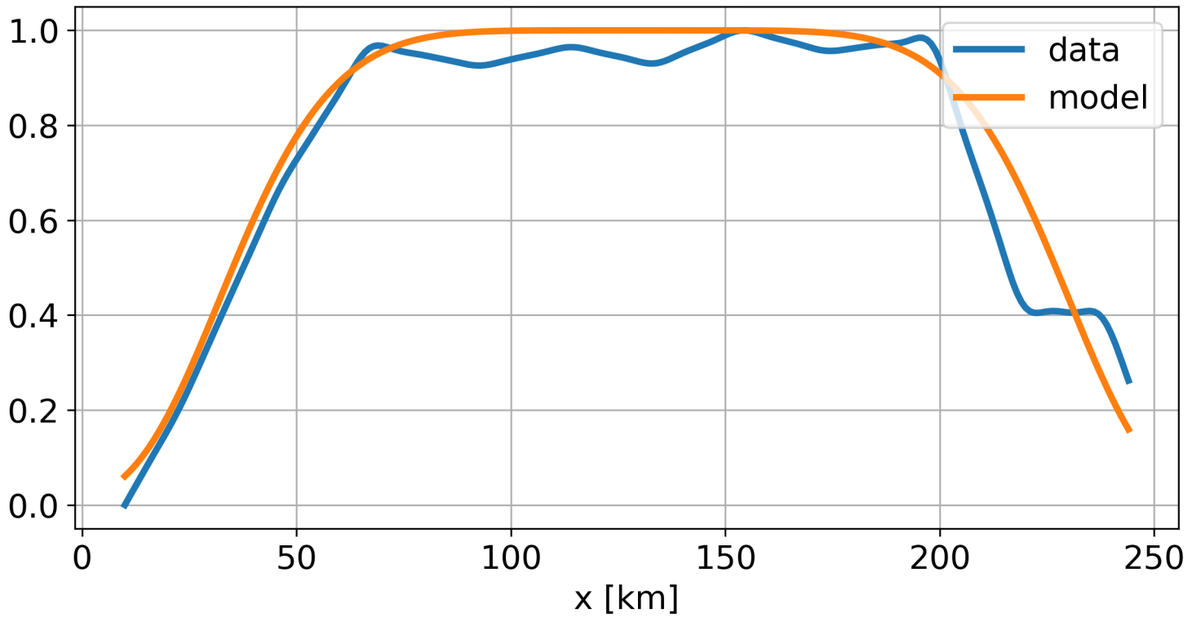

Figure 10.

(a) $RMS = 8.4\%$, $\xi_0 = -3e-2m$, $z_2 = -175m$, $H_2 = 62.4m$, $D = -1.5e-2m$

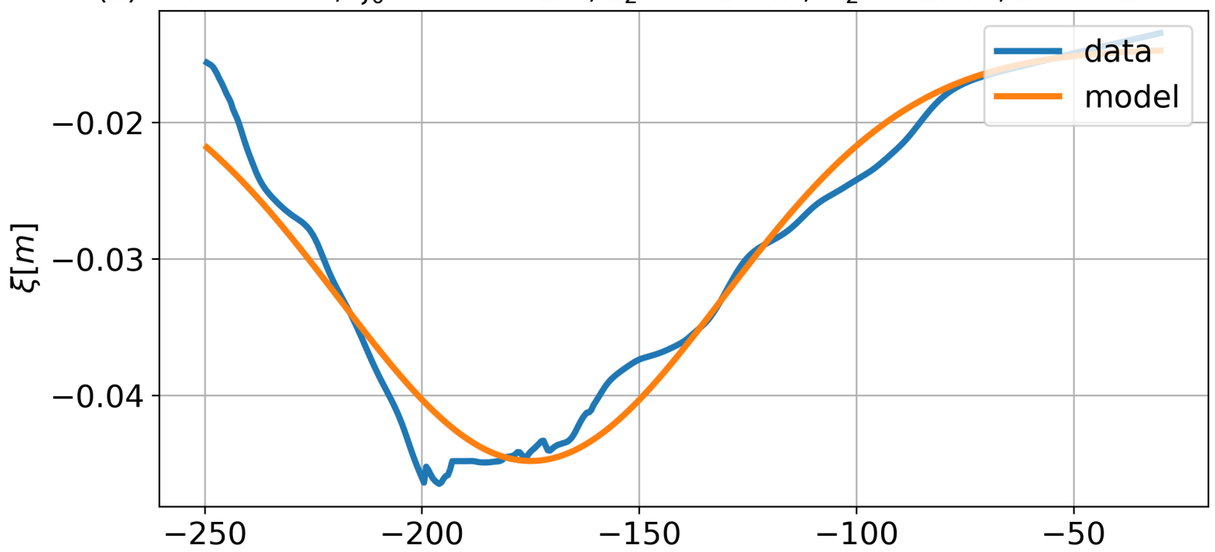

(b) $RMS = 3.83\%$, $\xi_0 = -3.8e-3m$, $z_2 = -254m$, $H_2 = 102m$, $D = -1e-2m$

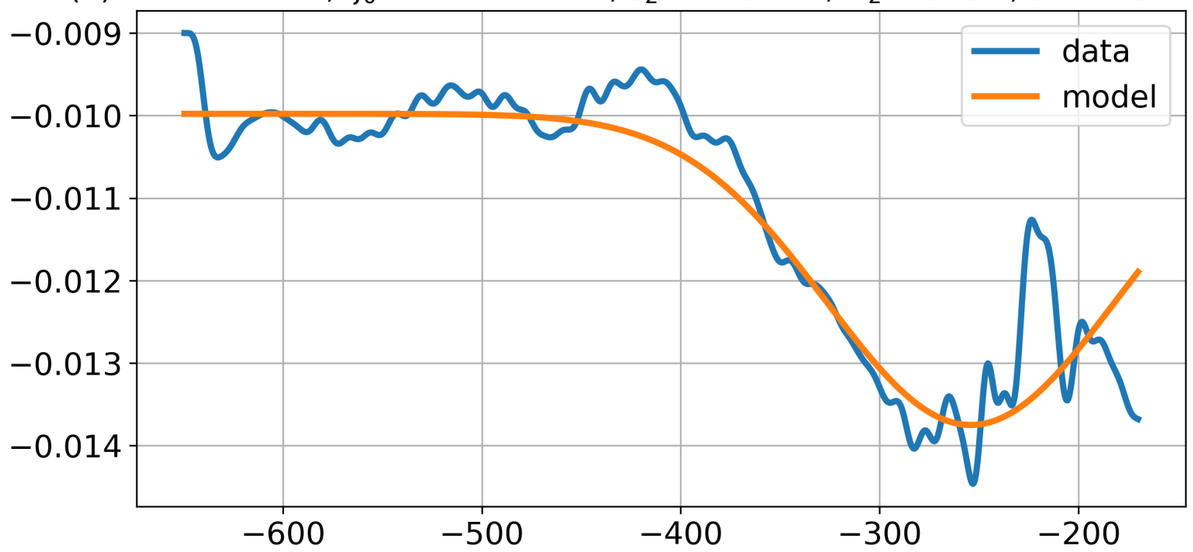

(c) $RMS = 8.4\%$, $\xi_0 = -8.5e-3m$, $z_2 = -118m$, $H_2 = 101m$, $D = -1.5e-1m$

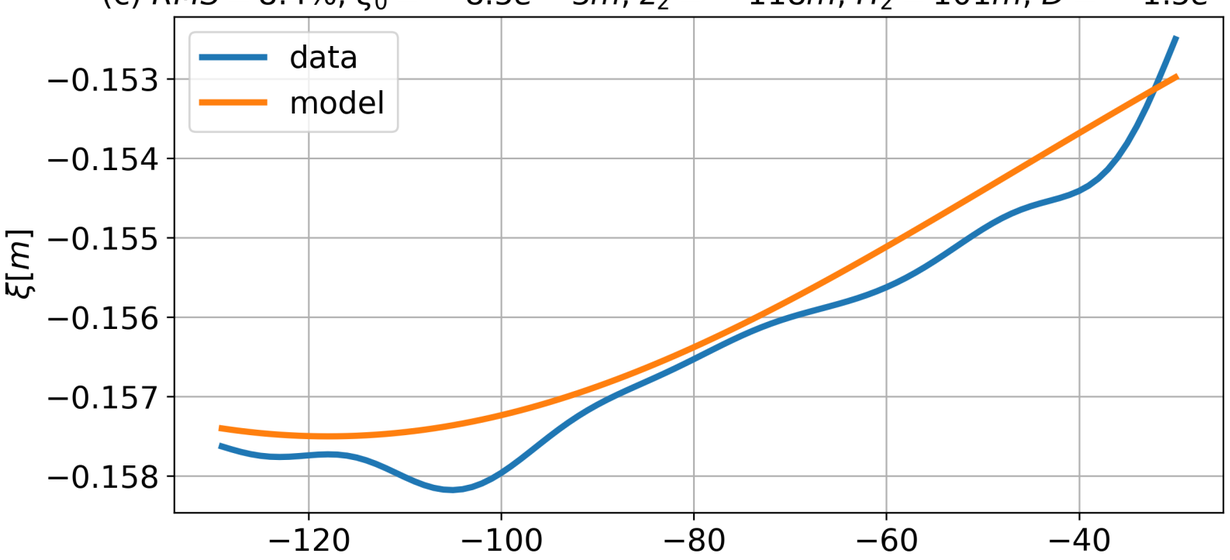

(d) $RMS = 7.5\%$, $\xi_0 = 4.6e-3m$, $z_2 = -121m$, $H_2 = 112$, $D = -1.5e-1m$

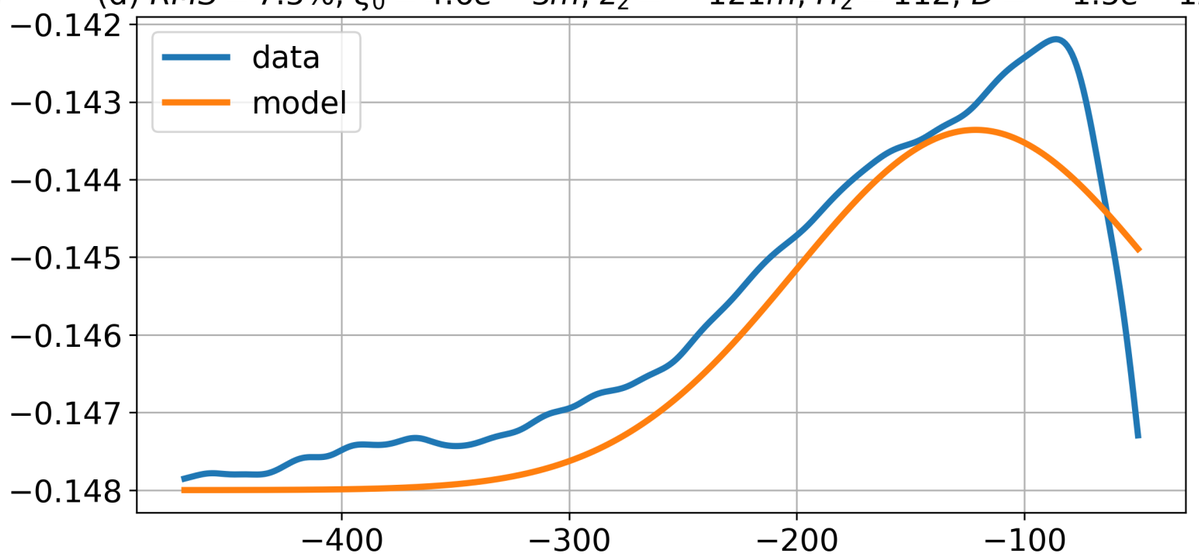

(e) $RMS = 9.5\%$, $\xi_0 = 5.7e-3m$, $z_2 = -127m$, $H_2 = 83.2m$, $D = -1.48e-1m$

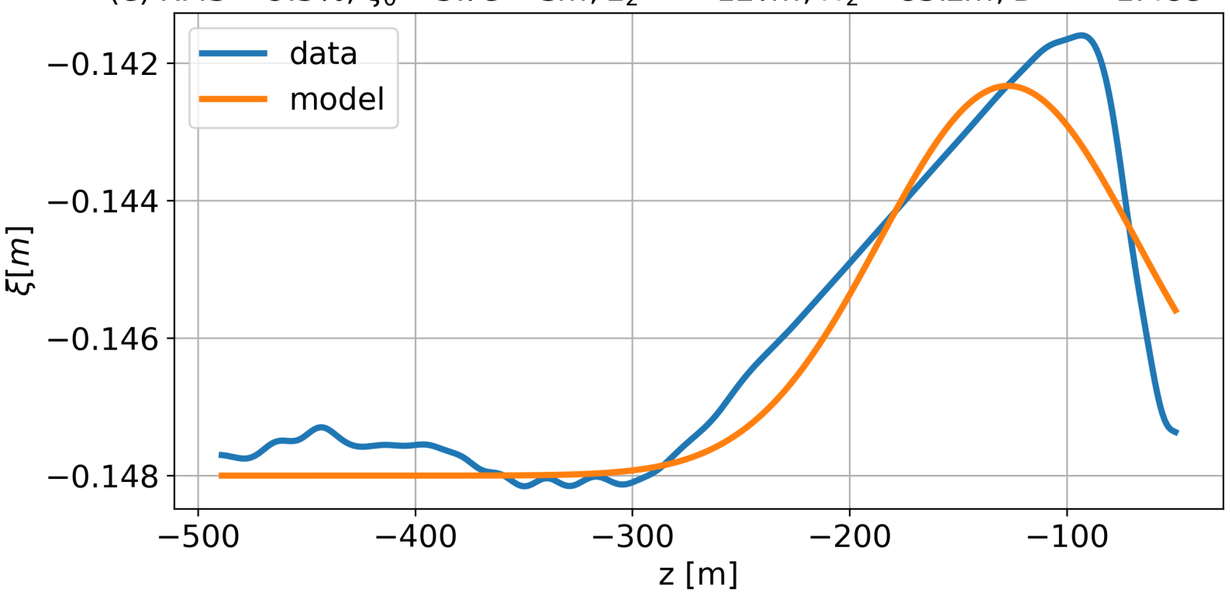

(f) $RMS = 4.83\%$, $\xi_0 = 5.9e-3m$, $z_2 = -109m$, $H_2 = 111m$, $D = -1.49e-1m$

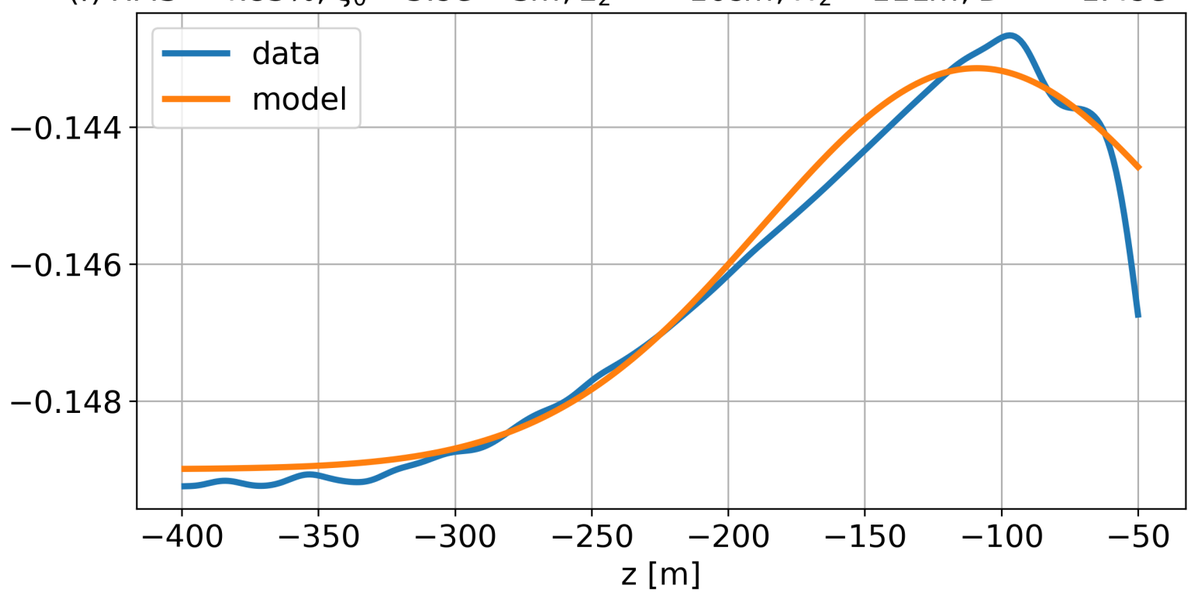

Figure 11.

(a) $RMS = 8.1\%$, $x_2 = 187km$, $R_2 = 97km$, $\alpha_2 = 2$

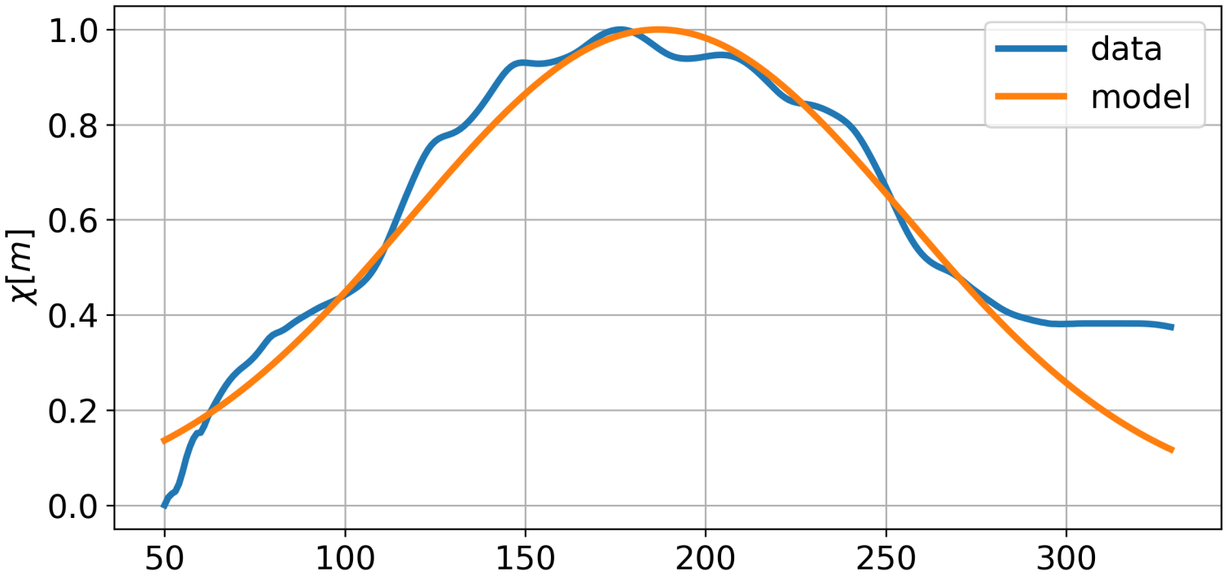

(b) $RMS = 6.7\%$, $x_2 = 98.4km$, $R_2 = 85.2km$, $\alpha_2 = 6$

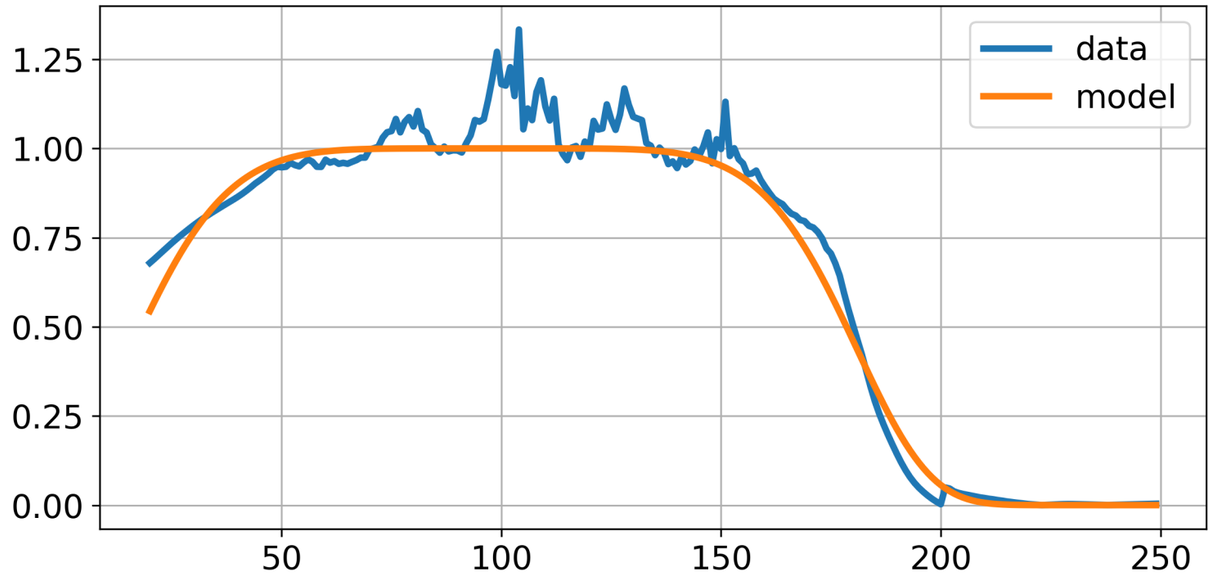

(c) $RMS = 9.4\%$, $x_2 = 461km$, $R_2 = 48.5km$, $\alpha_2 = 4$

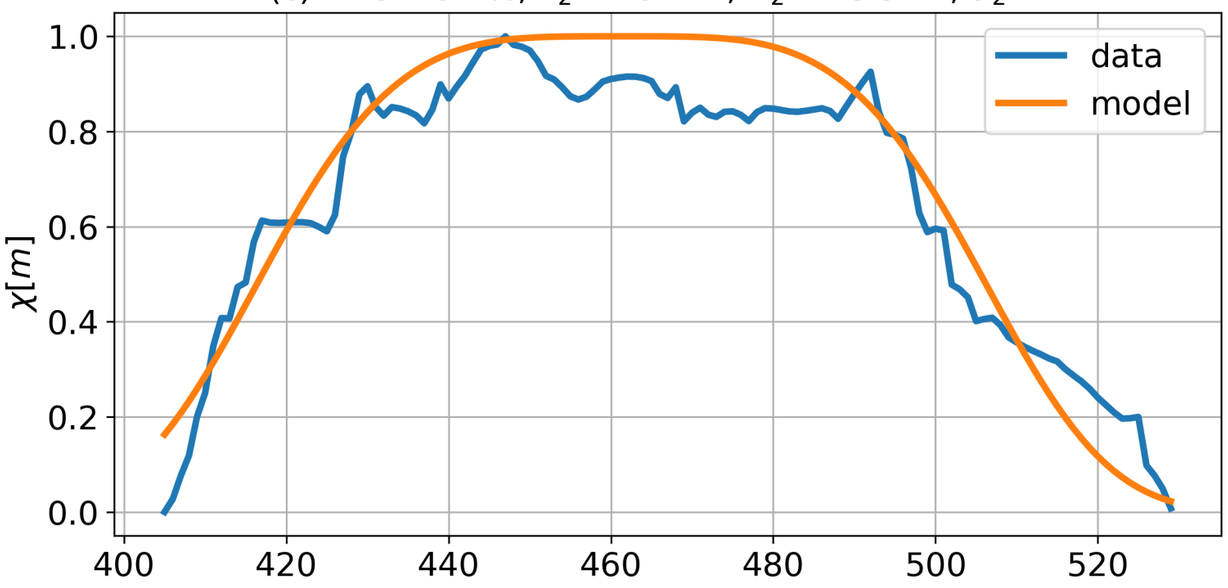

(d) $RMS = 6.9\%$, $x_2 = 72km$, $R_2 = 43km$, $\alpha_2 = 2$

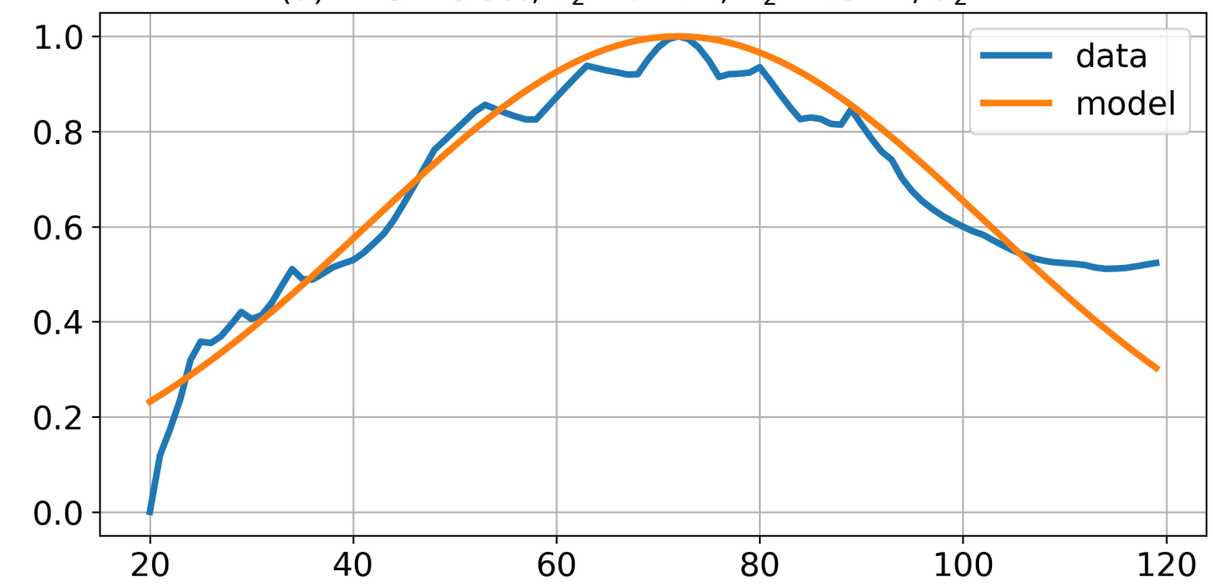

(e) $RMS = 8.1\%$, $x_2 = 50.2km$, $R_2 = 80.8km$, $\alpha_2 = 4$

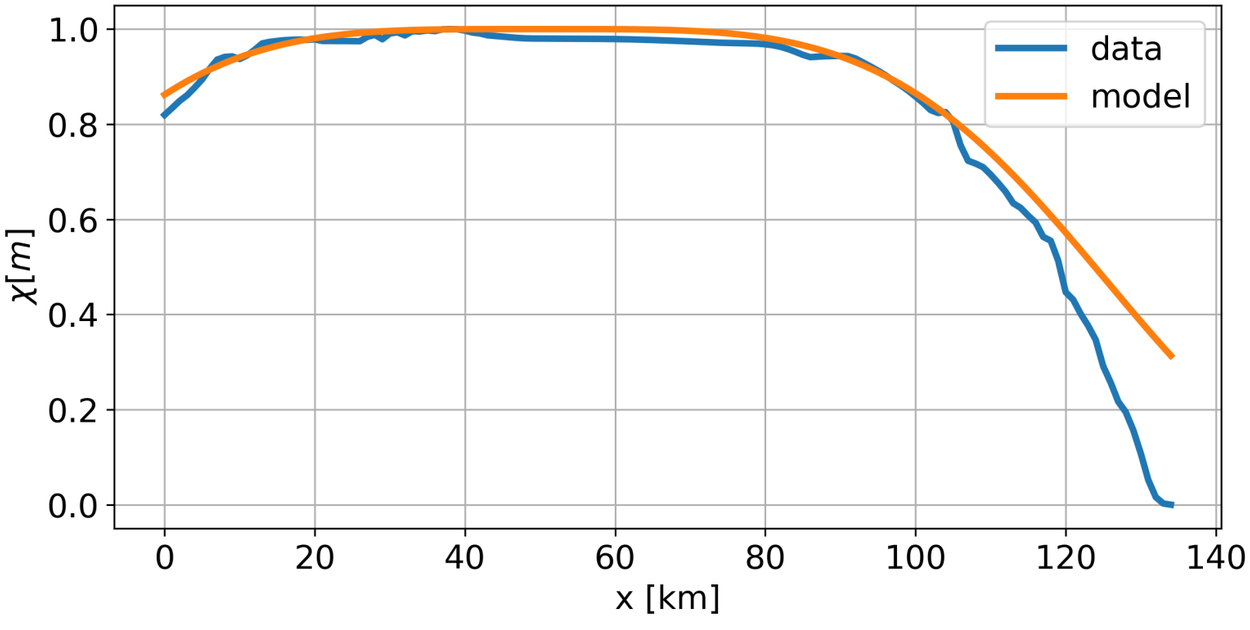

(f) $RMS = 9.4\%$, $x_2 = 130km$, $R_2 = 100km$, $\alpha_2 = 6$

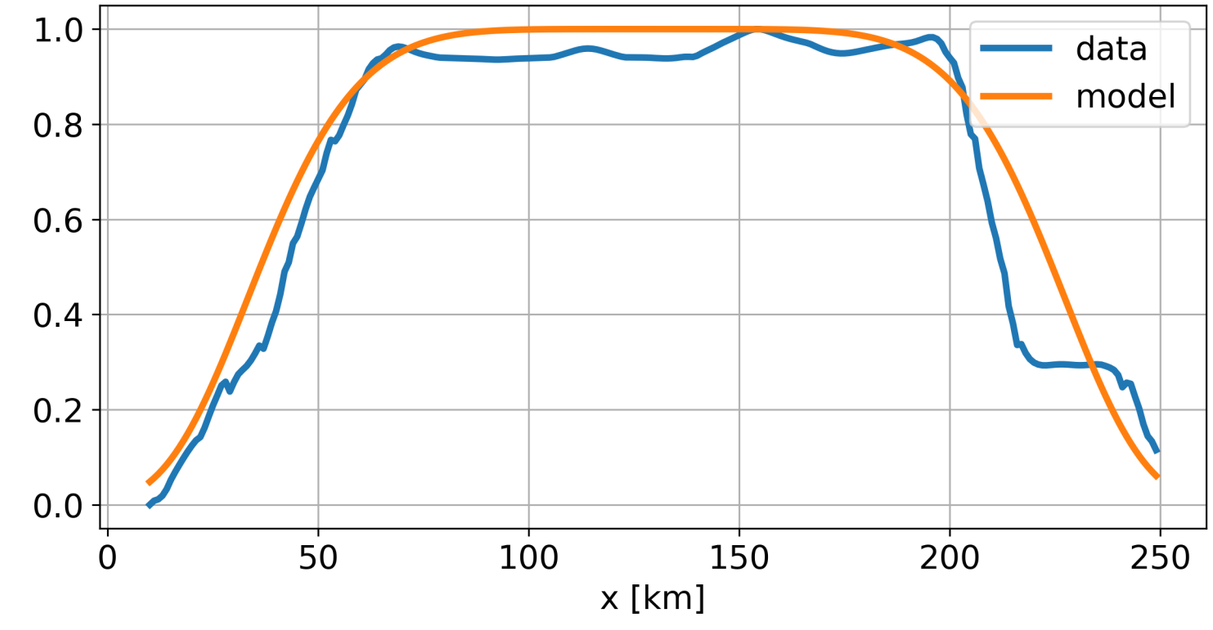

Figure 12.

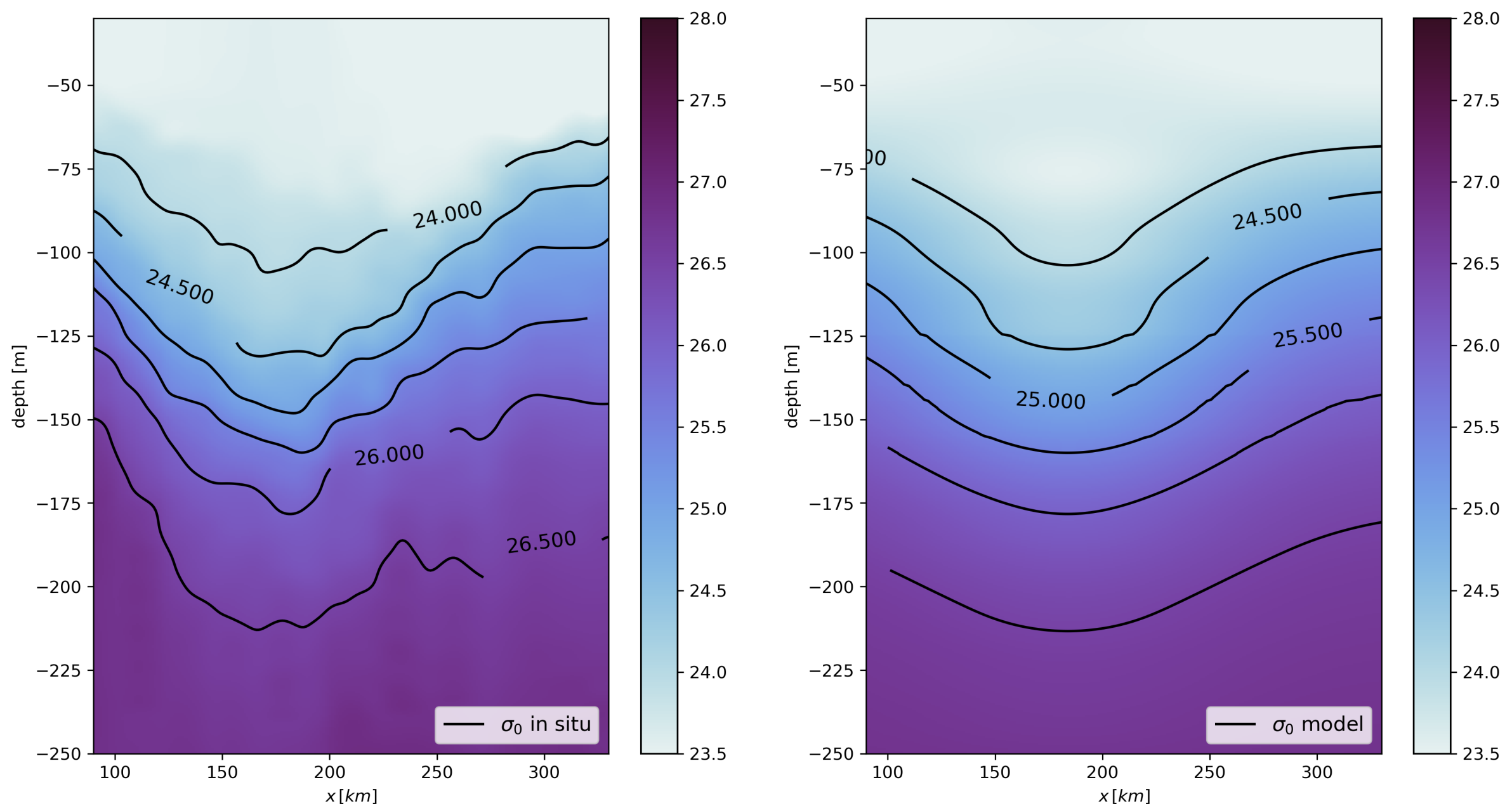
depth [m]
−50
−75
−100
−125
−150
−175
−200
−225
−250
100
150
200
250
300
x [km]
24.000
24.500
26.000
26.500
σ0 in situ
28.0
27.5
27.0
26.5
26.0
25.5
25.0
24.5
24.0
23.5
depth [m]
x [km]
24.500
25.000
25.500
σ0 model

Figure 13.

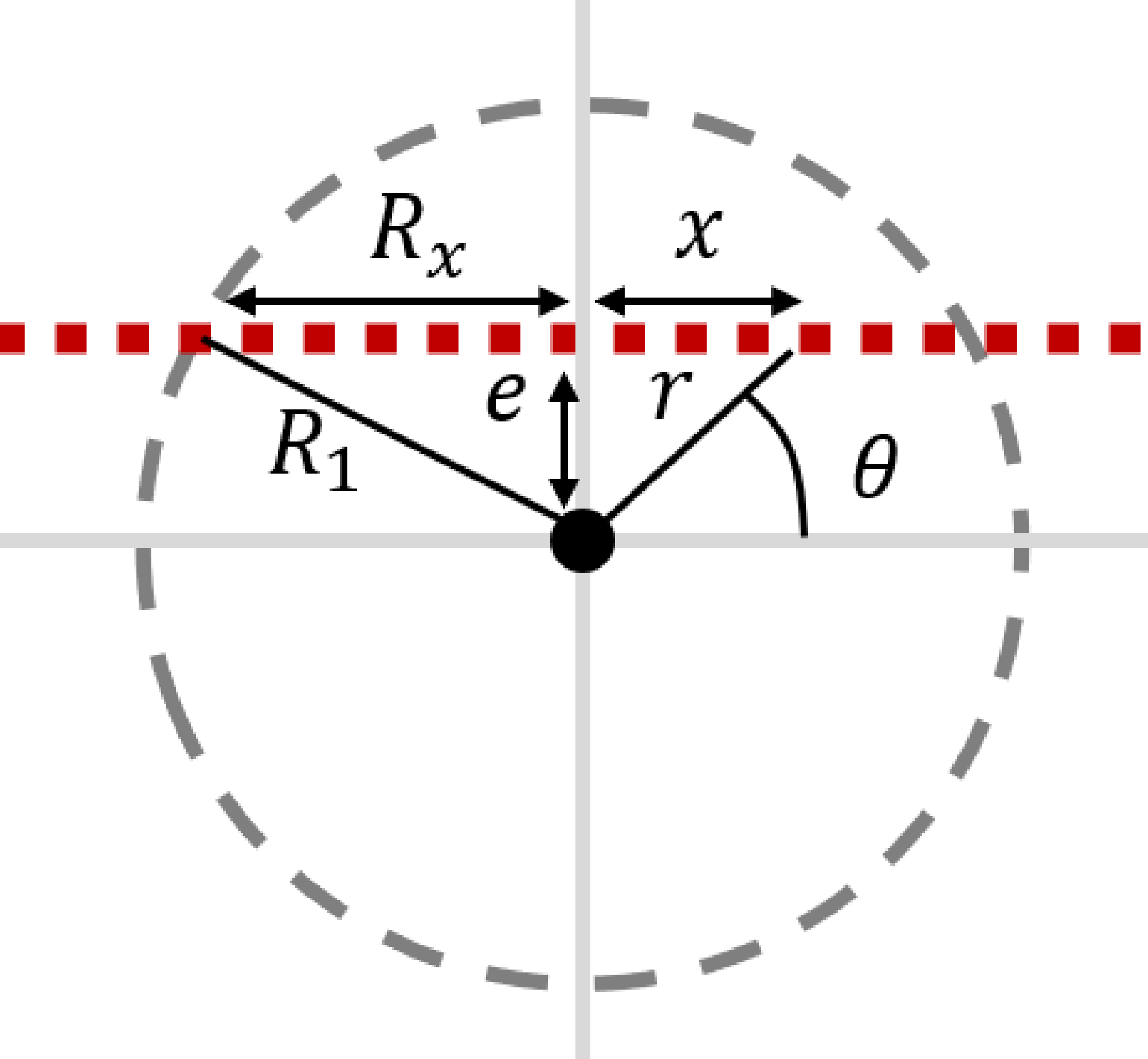
R_x
x
e
r
R_1
θ